

Solution Separation Versus Residual-Based RAIM

MATHIEU JOERGER, FANG-CHENG CHAN and BORIS PERVAN
Illinois Institute of Technology, Chicago, IL

Received February 2014; Revised June 2014

ABSTRACT: *Future multi-constellation Global Navigation Satellite Systems (GNSS) will offer the possibility to fulfill stringent navigation integrity requirements using Receiver Autonomous Integrity Monitoring (RAIM). This paper presents a detailed comparison of residual-based (RB) and solution separation (SS) RAIM. A complete step-by-step derivation of the two methods, which is currently missing in the literature, is given for the detection of single and multi-measurement faults, starting from common definitions of the integrity and continuity risks. In addition, a parity-space representation of SS RAIM is developed. It is shown that the integrity monitoring performance of SS RAIM can be superior to RB RAIM because SS test statistics are tailored to the fault hypotheses, and to the state of interest. However, for practical reasons of computational efficiency in conventional SS implementations, which are fully detailed in the paper, RB RAIM ultimately provides tighter bounds on integrity risk. Copyright © 2014 Institute of Navigation.*

INTRODUCTION

Global navigation satellite system (GNSS) measurements are vulnerable to faults, which can potentially lead to major integrity threats for users. To mitigate their impact, user fault detection algorithms such as receiver autonomous integrity monitoring (RAIM) can be implemented [1, 2]. Two RAIM methods in particular have been widely used over the past two decades in safety-critical applications: least-squares residual-based (RB) [2–4] and solution separation (SS) RAIM [1, 5]. These two methods have long been thought to be equivalent, but have only been roughly compared [6–8]. In this work, a rigorous step-by-step derivation of RB and SS RAIM is provided starting from a common definition of the integrity risk, which is the probability of undetected faults causing unacceptably large positioning errors.

The core principle of RAIM is to exploit redundant measurements to achieve self-contained fault detection at the user receiver. With the full deployment of GLONASS and with the emergence of Galileo and Beidou, an increased number of redundant ranging signals becomes available, which has recently drawn a renewed interest in RAIM. In particular, RAIM can help alleviate requirements

on ground monitors. For example, researchers in the European Union and in the United States are investigating Advanced RAIM (ARAIM) for world-wide vertical guidance of aircraft [9]. Challenges arise when using multi-constellation GNSS because of the substantial increase in probability of multiple simultaneous satellite faults, which must hence be detected.

In addition, RAIM not only aims at detecting faults but also at evaluating the integrity risk, or alternatively, a protection level, which is an integrity-bound on the position estimate error. Integrity risk evaluation is needed when designing a navigation system to meet predefined integrity requirements, and it is needed operationally to inform the user whether a mission should be pursued or aborted. Integrity risk evaluation includes both assessing the fault detection capability and quantifying the impact of undetected faults on estimation errors. In order to avoid making assumptions on unknown fault distributions, a bound on the integrity risk corresponding to the worst-case fault can be evaluated. This bound is then compared to a specified integrity risk requirement to assess availability, which is the fraction of time where position estimates can safely be used [10]. It is therefore of primary importance for system availability to derive a *tight bound* on the integrity risk.

In multi-constellation GNSS, two major issues must be addressed when assessing the tightness of

The peer review of this paper was independently handled by Dr. Jade Morton, Associate Editor for the *IEEE Transactions on Aerospace and Electronic Systems*.

NAVIGATION: *Journal of The Institute of Navigation*
Vol. 61, No. 4, Winter 2014
Printed in the U.S.A.

the integrity risk bounds for RB and SS RAIM. First, RB RAIM implementation is straightforward in that it uses a single test statistic for detection [6]. However, to evaluate integrity risk the ‘worst-case’ measurement fault vector, which maximizes the integrity risk, must be determined. In contrast, SS RAIM formulations are fully derived in the position domain [5, 7], which eliminates the need for determining the worst-case fault in the measurement domain. But SS RAIM is based on protection levels established using multiple test statistics – one for each fault hypothesis. Protection level derivations found in the literature (e.g., in [5, 7]) deal with the multiple SS test statistics, which are mutually correlated, by implicitly making key conservative assumptions. Unless these assumptions are clarified, and unless their impact is quantified, it remains unknown which of RB or SS RAIM provides the tightest integrity risk bound.

In response, this paper presents a complete measurement-level derivation of both RB and SS RAIM against single and multi-measurement faults. This approach sets fair grounds for an analytical comparison of the two methods. In particular, it provides the means to determine the conditions of their equivalence, and to identify, analyze, and evaluate their differences in terms of integrity monitoring performance. To support these findings, a graphical representation is developed, which enables simultaneous visualization of RB and SS detection boundaries.

A procedure is set forth to handle multiple fault hypotheses for integrity risk evaluation using multi-constellation GNSS. An analytical expression of the worst-case fault vector is established, which enables measurement-level integrity risk evaluation in the presence of faults affecting subsets of multiple satellites. This derivation goes beyond prior work in [11, 12], where the worst-case fault vector for RB RAIM was numerically determined by solving an eigenvector problem. Here, the impact of the worst-case fault on integrity risk using RB RAIM and SS RAIM is directly expressed in closed form in terms of the measurement noise covariance and observation matrices.

These tools are used to perform an analytical comparison between RB and SS RAIM. Contrary to the colloquial understanding, it is shown that the two methods have fundamental differences. In particular, under the simplified scenario that only one satellite subset can potentially be faulted and all others are fault-proof, it is shown that the integrity risk is lower using SS than using RB RAIM because, unlike in RB RAIM, the SS detection test statistics are tailored to the fault mode and to the state of interest. This observation remains true for more realistic scenarios where satellites have more than one way of failing. In this regard, recent publications

in [13, 14] have suggested that SS test statistics provide a closer approximation of the optimal detector than RB RAIM. (In [13, 14], the optimal detector is numerically determined by solving a convex integrity risk minimization problem.)

Then, a ‘parity-space’ representation is employed, which was introduced in [3] for RB fault detection. The parity vector is the simplest, most fundamental expression of the detection capability. It is well known that the norm of the parity vector is equal to the RB test statistic [3, 4]. But it is also proven in this paper that for single-satellite faults, the SS test statistics are projections of the parity vector on fault mode lines. It follows that the detection boundaries in parity space are a hyper-sphere for RB RAIM and a polytope for SS RAIM.

Given this understanding of the detection boundaries, the paper then explains the conservative assumptions that must be made in SS RAIM to enable integrity risk evaluation. Parity-space representations provide graphical interpretations for the main steps of the SS RAIM integrity risk bounding process. This bounding process is steered by practical considerations, leading to conservative assumptions, which are exposed as the major source of difference in integrity risk bounding between RB and SS RAIM.

Finally, a performance analysis is carried out for an example application of aircraft positioning during final approach. The sensitivity of integrity risk bounds for RB and SS RAIM are first analyzed as functions of alert limit and continuity risk requirements, and then compared for multiple GPS and GPS/Galileo satellite geometries. The results show that RB RAIM can provide a tighter integrity risk bound than SS RAIM, but this advantage comes at the cost of a higher computation load to determine the worst-case measurement fault.

INTEGRITY AND CONTINUITY RISK EVALUATION

This section outlines a multiple-hypothesis integrity risk evaluation method, which involves quantifying the impact of undetected faults on the estimation error. The integrity and continuity risks are first defined, followed by a model of the measurements, which are then used to determine the estimation error. The content of this section is used in the remainder of the paper to analyze both SS and RB detection methods.

Integrity and Continuity Risk Definitions

The integrity risk, or equivalently the probability of hazardous misleading information (HMI), is a joint probability defined as:

$$P_{HMI} = P(|\varepsilon_0| > \ell \cap |q| < T) \quad (1)$$

where

- ε_0 is the estimation error on the parameter of interest, referred to as ‘state’ of interest
- ℓ is a specified alert limit that defines hazardous situations (e.g., specified in [9, 10] for aircraft approach navigation)
- q is the detection test statistic
- T is the detection threshold

The random variables ε_0 and q are further described in the following sections.

A multiple-hypothesis approach is employed, which accounts for all faulty space vehicle (SV) combinations. First, consider a set of events, which is made of all fault combinations affecting a minimum number of SVs noted n_{MIN} . Let $P_{>n_{MIN}}$ be the prior probability of occurrence of more than n_{MIN} simultaneous faults, and let I_{REQ} be the integrity risk requirement. Appendix A shows that if n_{MIN} is selected such that $P_{>n_{MIN}}$ is much smaller than I_{REQ} , then $P_{>n_{MIN}}$ can directly be subtracted from I_{REQ} . Then, let $h+1$ be the number of remaining fault hypotheses noted H_i , for $i=0, \dots, h$. Given this set of mutually exclusive, jointly exhaustive hypotheses, the law of total probability can be used to express the integrity criterion as:

$$\sum_{i=0}^h P(|\varepsilon_0| > \ell \cap |q| < T | H_i) P_{Hi} \leq I_{REQ} - P_{>n_{MIN}} \quad (2)$$

where

- P_{Hi} is the prior probability of H_i occurrence
- H_0 is the fault-free hypothesis
- H_i for $i=1, \dots, h$ are the fault hypotheses corresponding to faults on subset measurement ‘ i ’ (including single-SV and multi-SV faults)

In addition, let T be the detection threshold and let C_{REQ} be a continuity risk requirement allocation (e.g., specified in [9, 10] for aviation applications) set to limit the probability of false alarms. Under the fault-free hypothesis H_0 , T can be defined as [15]:

$$P(|q| \geq T | H_0) P_{H0} \leq C_{REQ} \quad (3)$$

The left-hand side term in Equation (3) is typically referred to as continuity risk in fault-detection papers (including this one), although it only accounts for false alarms. The full continuity risk actually takes into account all mission interruptions, including alarms under H_i for $i \neq 0$. But, limiting the impact of such events requires fault exclusion, which is beyond the scope of this paper.

Measurement Equation

The estimate error ε_0 and test statistic q in Equation (2) are evaluated using a measurement model. Let n and m respectively be the numbers of

measurements and of parameters to be estimated (i.e., the ‘states’) and let \mathbf{z}_* be the $n \times 1$ vector of stacked measurements. This work assumes that the cumulative distribution function of nominal measurement errors is bounded by a zero mean Gaussian distribution with a positive definite covariance matrix \mathbf{V}_* [16]. Vector \mathbf{z}_* is pre-multiplied by $\mathbf{V}_*^{-1/2}$ to obtain the ‘normalized’ measurement equation:

$$\mathbf{z} = \mathbf{H}\mathbf{x} + \mathbf{v} + \mathbf{f} \quad (4)$$

where

- $\mathbf{z} = \mathbf{V}_*^{-1/2} \mathbf{z}_*$ is the normalized measurement vector
- \mathbf{H} is the $n \times m$ normalized observation matrix
- \mathbf{x} is the $m \times 1$ state vector
- \mathbf{f} is the $n \times 1$ normalized fault vector.
- \mathbf{v} is the $n \times 1$ normalized measurement noise vector composed of zero-mean, unit-variance independent and identically distributed (i.i.d.) random variables.

We use the notation:

$$\mathbf{v} \sim N(\mathbf{0}_{n \times 1}, \mathbf{I}_n) \quad (5)$$

where

- $\mathbf{0}_{a \times b}$ is a $a \times b$ matrix of zeros (in this case, it is an $n \times 1$ vector of zeros)
- \mathbf{I}_n is an $n \times n$ identity matrix

In order to avoid making assumptions on unknown fault distributions, a bound on the probability of HMI can be evaluated for the worst-case $n \times 1$ fault vector $\bar{\mathbf{f}}_i$ under H_i :

$$P(|\varepsilon_0| > \ell \cap |q| < T | H_i) \leq P(|\varepsilon_0| > \ell \cap |q| < T | H_i \cap \bar{\mathbf{f}}_i) \quad (6)$$

Vector $\bar{\mathbf{f}}_i$ can be interpreted as a vector of deterministic measurement biases. Although the actual fault \mathbf{f} is unknown, the worst case fault vector $\bar{\mathbf{f}}_i$, which maximizes the integrity risk given H_i , is analytically derived later in this paper.

Under hypothesis H_i , let n_i be the number of measurements impacted by the fault, i.e., the number of non-zero elements in \mathbf{f} . One fundamental limitation of RAIM is that if n_i is larger than the number of redundant signals ($n-m$), then the fault may be undetectable [3]. Therefore, for RAIM to be effective, n_i must always satisfy the following inequality:

$$n_i \leq n - m \quad (7)$$

Equation (7) is assumed to be true throughout the paper.

Least-Squares Estimation

In this paper, we consider a least-squares estimator. Let \mathbf{a} be a $m \times 1$ vector used to extract the state of interest ‘ x ’ (e.g., the vertical position coordinate is often of primary concern for aircraft precision approach navigation) out of the full state vector:

$$\boldsymbol{\alpha}^T = \begin{bmatrix} \mathbf{0}_{m_A \times 1}^T & 1 & \mathbf{0}_{m_B \times 1}^T \end{bmatrix} \quad (8)$$

where, in the order in which states are stacked in \mathbf{x} , m_A and m_B are the numbers of states respectively before and after state x . Assuming that \mathbf{H} is full rank and that $n \geq m$, the least-squares estimate of state x is defined as:

$$\hat{x}_0 \equiv \mathbf{s}_0^T \mathbf{z} \quad (9)$$

where

$$\mathbf{s}_0^T = \boldsymbol{\alpha}^T \mathbf{S}_0, \mathbf{S}_0 = \mathbf{P}_0 \mathbf{H}^T \text{ and } \mathbf{P}_0 = (\mathbf{H}^T \mathbf{H})^{-1} \quad (10)$$

The estimate error appearing in the integrity risk Equation (2) is defined as:

$$\varepsilon_0 \equiv \hat{x}_0 - x = \mathbf{s}_0^T (\mathbf{v} + \mathbf{f}) \quad (11)$$

$$\varepsilon_0 \sim N(\mathbf{s}_0^T \mathbf{f}, \sigma_0^2 \equiv \boldsymbol{\alpha}^T \mathbf{P}_0 \boldsymbol{\alpha}) \quad (12)$$

In the next section, we analyze two of the most widely-implemented detection methods in RAIM: residual-based (RB) and solution separation (SS) RAIM.

BASELINE RAIM DETECTION TEST STATISTICS

Residual-Based RAIM

The residual vector is defined as [2, 3]:

$$\mathbf{r} \equiv (\mathbf{I}_n - \mathbf{H} \mathbf{S}_0) \mathbf{z} = (\mathbf{I}_n - \mathbf{H} \mathbf{S}_0) (\mathbf{v} + \mathbf{f}) \quad (13)$$

The residual-based test statistic q_{RB} is the norm of the residual (weighted by $\mathbf{V}^{-1} = \mathbf{I}$):

$$q_{RB}^2 \equiv \mathbf{r}^T \mathbf{r} \quad (14)$$

The scalar random variable q_{RB}^2 follows a non-central chi-square distribution with $(n-m)$ degrees of freedom and non-centrality parameter λ_{RB}^2 [3]. The following notation is used:

$$q_{RB}^2 \sim \chi^2(n-m, \lambda_{RB}^2) \quad (15)$$

Where

$$\lambda_{RB}^2 = \mathbf{f}^T (\mathbf{I}_n - \mathbf{H} \mathbf{S}_0) \mathbf{f} \quad (16)$$

Solution Separation RAIM

Without loss of generality (because the order in which measurements are stacked in \mathbf{z} is arbitrary), it is assumed that under a fault hypothesis H_i , the faulty measurements are the first n_i elements of \mathbf{z} . The measurement Equation (4) can be partitioned to distinguish the subset of potentially faulty measurements $\mathbf{A}_i^T \mathbf{z}$ from the fault-free measurements $\mathbf{B}_i^T \mathbf{z}$:

$$\begin{bmatrix} \mathbf{A}_i^T \mathbf{z} \\ \mathbf{B}_i^T \mathbf{z} \end{bmatrix} = \begin{bmatrix} \mathbf{A}_i^T \mathbf{H} \\ \mathbf{B}_i^T \mathbf{H} \end{bmatrix} \mathbf{x} + \begin{bmatrix} \mathbf{A}_i^T \mathbf{v} \\ \mathbf{B}_i^T \mathbf{v} \end{bmatrix} + \begin{bmatrix} \mathbf{A}_i^T \mathbf{f} \\ \mathbf{0}_{(n-n_i) \times 1} \end{bmatrix} \quad (17)$$

With

$$\mathbf{A}_i \equiv \begin{bmatrix} \mathbf{I}_{n_i} \\ \mathbf{0}_{(n-n_i) \times n_i} \end{bmatrix} \text{ and } \mathbf{B}_i \equiv \begin{bmatrix} \mathbf{0}_{n_i \times (n-n_i)} \\ \mathbf{I}_{n-n_i} \end{bmatrix} \quad (18)$$

The measurement vector partition in Equation (17) is employed to distinguish the full-set solution \hat{x}_0 in Equation (9), obtained using all n measurements, from the subset solution \hat{x}_i , derived using only the $(n-n_i)$ fault-free measurements under H_i . Under the assumption already stated in Equation (7) that $n-n_i \geq m$, and assuming that $\mathbf{B}_i^T \mathbf{H}$ is full rank, \hat{x}_i is defined as:

$$\hat{x}_i \equiv \mathbf{s}_i^T \mathbf{z}, \text{ for } i = 1, \dots, h \quad (19)$$

where

$$\mathbf{s}_i^T = \boldsymbol{\alpha}^T \mathbf{S}_i, \mathbf{S}_i = \mathbf{P}_i \mathbf{H}^T \mathbf{B}_i \mathbf{B}_i^T \text{ and } \mathbf{P}_i = (\mathbf{H}^T \mathbf{B}_i \mathbf{B}_i^T \mathbf{H})^{-1} \quad (20)$$

It follows that, under H_i , the estimate error ε_i is given by:

$$\varepsilon_i \equiv \mathbf{s}_i^T (\mathbf{v} + \mathbf{f}) = \mathbf{s}_i^T \mathbf{v} \quad (21)$$

$$\varepsilon_i \sim N(0, \sigma_i^2 \equiv \boldsymbol{\alpha}^T \mathbf{P}_i \boldsymbol{\alpha}) \quad (22)$$

Thus, subscript ‘ i ’ identifies fault hypothesis H_i and designates its corresponding fault-free subset solution ε_i (obtained by removing measurement subset i). In parallel, the double usage of subscript ‘0’ is worth clarifying: ‘0’ indicates the fault-free hypothesis H_0 , and it is also used to designate the full-set positioning solution ε_0 (obtained by removing the empty subset 0), which is computed under all hypotheses, but is not fault-free under H_i for $i \neq 0$.

The solution separations are defined as [1, 5]:

$$\Delta_i \equiv \hat{x}_0 - \hat{x}_i = \varepsilon_0 - \varepsilon_i, \text{ for } i = 1, \dots, h \quad (23)$$

Δ_i can also be expressed as:

$$\Delta_i = \mathbf{s}_{\Delta i}^T \mathbf{z} \text{ and } \Delta_i \sim N(\mathbf{s}_{\Delta i}^T \mathbf{f}, \sigma_{\Delta i}^2) \text{ with } \sigma_{\Delta i}^2 = \boldsymbol{\alpha}^T \mathbf{P}_{\Delta i} \boldsymbol{\alpha} \quad (24)$$

where

$$\mathbf{s}_{\Delta i} = \mathbf{s}_0 - \mathbf{s}_i \quad (25)$$

and Appendix B presents a derivation in matrix form for the following result (a scalar-form derivation is given in [7]):

$$\mathbf{P}_{\Delta i} = \mathbf{P}_i - \mathbf{P}_0, \text{ hence } \sigma_{\Delta i}^2 = \sigma_i^2 - \sigma_0^2 \quad (26)$$

Later in this paper, the section entitled “Practical Approach to SS RAIM” will use Δ_i as the SS test statistic, which is typical in conventional SS algorithms. But, in the next sections, an *equivalent* SS test statistic q_i is employed, which yields the exact same performance in terms of integrity and continuity risks and also facilitates direct comparison with q_{RB} . The equivalent SS test statistics are ‘normalized’ solution separations, which are defined as:

$$q_i \equiv \Delta_i / \sigma_{\Delta_i}, \text{ for } i = 1, \dots, h \quad (27)$$

$$q_i^2 \sim \chi^2(1, \lambda_i^2) \text{ with } \lambda_i^2 = \mathbf{f}^T \mathbf{s}_{\Delta_i} \mathbf{s}_{\Delta_i}^T \mathbf{f} / \sigma_{\Delta_i}^2 \quad (28)$$

Appendix C shows that both q_{RB} and q_i (or Δ_i) are derived from vectors lying in the null space of \mathbf{H}^T , also called parity space. In the same appendix, it is also proved that using a least-squares estimator, and for *any* test statistic q lying in the parity space, the estimate error ε_0 and q are statistically independent, so that the joint probability in Equation (6) can be expressed as:

$$\begin{aligned} P(|\varepsilon_0| > \ell | q| < T | H_i \cap \bar{\mathbf{f}}_i) \\ = P(|\varepsilon_0| > \ell | H_i \cap \bar{\mathbf{f}}_i) P(|q| < T | H_i \cap \bar{\mathbf{f}}_i) \end{aligned} \quad (29)$$

All the variables and parameters in Equation (29) have been fully described, except for the worst-case fault vector $\bar{\mathbf{f}}_i$ which is derived in the following section.

RAIM AGAINST MULTI-MEASUREMENT FAULTS

In order to compare RB versus SS RAIM in the presence of multiple simultaneous faults, the worst-case fault vector $\bar{\mathbf{f}}_i$ must be determined for both RAIM methods. The term ‘worst-case’ indicates that the fault vector $\bar{\mathbf{f}}_i$ maximizes the integrity risk bound for a given hypothesis H_i .

In general, a fault vector \mathbf{f} can be characterized by:

- the fault hypothesis also called *fault mode*, which identifies the subset of satellites affected by the fault (captured by H_i in Equation (29)),
- the fault *magnitude*, which is the Euclidean norm of the fault vector, and
- the fault *direction*, which is determined by the relative values of the fault vector’s elements.

Figure 1 presents example fault vectors. The first group of vectors includes single-SV fault vectors, modeling fault modes on the first, second and n^{th} satellites (respectively named SV1, SV2, and SVn). For single-SV faults, it can be noted that the fault direction is fully defined by the fault mode and fault magnitude. This is not the case for multiple simultaneous satellite faults. For example, the

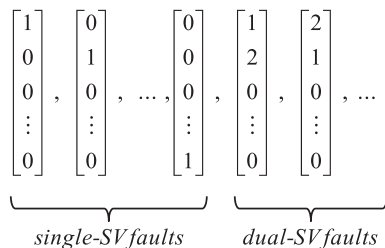


Fig. 1-Example Fault Vectors

last two vectors are both cases of dual-SV faults simultaneously affecting SV1 and SV2. Their modes and magnitudes are the same, but their direction is different.

Therefore, in the presence of multiple simultaneous faults, which are likely to occur in multi-constellation GNSS, it is not only crucial to determine the worst case fault magnitude (as for single SV faults), but it is also essential to derive the worst-case fault direction.

For single-SV faults, the worst-case fault magnitude is typically determined in RB RAIM using a straightforward search routine [17]. However, the same type of approach is not easily adapted to finding the worst-case fault direction, which is a multi-dimensional problem. In response, this section provides analytical solutions for RB and SS RAIM.

As expressed in Equations (12), (16), and (28), the fault vector \mathbf{f} impacts the mean of ε_0 and the non-centrality parameters of q_{RB} and q_i . It has been shown in [11, 12] that the worst case fault direction, which maximizes the integrity risk, is the one that maximizes the failure mode slope g_F . The square of the failure mode slope, which is independent of the fault magnitude, is defined as the ratio of the squared mean of the estimate error over the non-centrality parameter of the test statistic. g_F^2 can be expressed as:

$$g_F^2 \equiv \frac{\mathbf{f}^T \mathbf{s}_0 \mathbf{s}_0^T \mathbf{f}}{\mathbf{f}^T \mathbf{M}_D \mathbf{f}} \quad (30)$$

where the $n \times n$ matrix \mathbf{M}_D is defined as:

$$\begin{aligned} \mathbf{M}_D &= (\mathbf{I}_n - \mathbf{H}\mathbf{S}_0) & \text{for RB RAIM} \\ \mathbf{M}_D &= \mathbf{s}_{\Delta_i} \mathbf{s}_{\Delta_i}^T / \sigma_{\Delta_i}^2 & \text{for SS RAIM} \end{aligned}$$

Equation (30) is used in Appendix D to show that, given a fault mode H_i , the fault slope g_{Fi} is independent of fault direction for SS RAIM [18], and is given by:

$$g_{Fi}^2 = \sigma_{\Delta_i}^2 \quad (31)$$

where $\sigma_{\Delta_i}^2$ is the variance of the solution separation defined in (24). In addition, Appendix D proves that for RB RAIM, the worst-case failure mode slope and the corresponding worst-case fault vector direction are respectively given by:

$$\bar{g}_{Fi}^2 = \mathbf{m}_{Xi}^T (\mathbf{A}_i^T (\mathbf{I}_n - \mathbf{H}\mathbf{S}_0) \mathbf{A}_i)^{-1} \mathbf{m}_{Xi} \quad (32)$$

$$\bar{\mathbf{f}}_i = \mathbf{A}_i (\mathbf{A}_i^T (\mathbf{I}_n - \mathbf{H}\mathbf{S}_0) \mathbf{A}_i)^{-1} \mathbf{m}_{Xi} \quad (33)$$

where

\mathbf{A}_i is defined in Equation (18)

$$\mathbf{m}_{Xi} = \mathbf{A}_i^T \mathbf{s}_0$$

Equations (31) and (32) define the worst case fault slopes for SS and RB RAIM, respectively. The worst-case fault magnitude can then be determined

using a line search method (same treatment as for single-SV faults in RB RAIM).

The next section of this paper will further show that the worst case failure mode slope \bar{g}_{Fi} is actually the same for SS and RB RAIM, and that its value is $\sigma_{\Delta i}$. Equations (32) and (33) are essential, not only for the analytical comparison carried out in the next section, but also in general for direct integrity risk evaluation using RB RAIM in the presence of multi-measurement faults. Direct risk evaluation for SS RAIM can also be performed using Equation (31), but a more practical approach (detailed later in this paper) is typically implemented.

COMPARISON UNDER SINGLE-HYPOTHESIS SCENARIO

When comparing the two detection methods, the first difference to point out is that RB RAIM is based on a single test statistic q_{RB} , whereas SS uses as many test statistics q_i as fault hypotheses H_i , for $i=1, \dots, h$. Because the test statistics q_i are correlated, precise integrity risk evaluation using SS RAIM is exacting, and will require conservative approximations described in the next two sections.

But first, in this section, a rigorous comparison between RB and SS RAIM is achieved considering the theoretical, simplified scenario of one single hypothesis H_i , which can still be either a single-SV fault or a multi-SV fault. This scenario is as if all satellites were fault-proof except for one possibly faulted SV subset (the objective is to evaluate the integrity risk using all satellites). In this section, the subscript '1' replaces 'i' to remind the reader of the single hypothesis assumption:

H_i becomes H_1 .

In this case, both RB and SS RAIM use a single test statistic. This approach will reveal fundamental differences between the two methods.

Condition for Equivalence

This paragraph shows that, contrary to the colloquial understanding, the conditions for the equivalence of RB and SS RAIM are restricted to a particular set of assumptions. In Appendix E, a direct analytical comparison of q_{RB} versus q_1 under H_1 shows that RB and SS RAIM are equivalent if and only if:

$$n_1 = n - m = 1 \quad (34)$$

In other words, the two methods are equivalent under H_1 if and only if a single redundant measurement is available ($n - m = 1$) under a single-SV fault hypothesis ($n_1 = 1$). Therefore, in general, RB and SS RAIM are not equivalent. The remainder of this section aims at identifying which

of q_{RB} or q_1 generates the smallest integrity risk in the more general case.

Fundamental Differences Between RB and SS RAIM

Appendix F proves for single-SV and multi-SV faults ($n_1 \geq 1$), that the worst-case fault slope \bar{g}_{F1} is the same for RB and SS, and that:

$$\bar{g}_{F1}^2 = \sigma_{\Delta 1}^2 \quad (35)$$

The appendix further shows that for $n_1 = 1$, $\sigma_{\Delta 1}$ is actually the smallest worst-case fault slope value that any detector derived from the parity space can achieve.

Then, as expressed in Equations (15) and (28), it can be noted that q_{RB}^2 and q_1^2 both follow non-central chi-square distributions. But, the one fundamental difference is that the numbers of degrees of freedom of q_{RB}^2 and q_1^2 respectively are $n - m$ and 1.

This difference in number of degrees of freedom has an impact on the detection thresholds, which can vary greatly from one method to the other. As described in Equation (3), the detection thresholds T_{RB} and T_1 are set in compliance with a continuity risk requirement C_{REQ} to limit the probability of alarms under fault-free conditions (i.e., when the non-centrality parameter is zero). T_{RB} and T_1 are respectively defined as:

$$\int_{T_{RB}^2}^{+\infty} \chi_q^2(n - m, 0) dq = C_{REQ} \quad (36)$$

$$\int_{T_1^2}^{+\infty} \chi_q^2(1, 0) dq = C_{REQ} \quad (37)$$

Assuming that the following inequality is true (which is guaranteed using multi-constellation GNSS):

$$n - m \geq 1 \quad (38)$$

then, it follows that:

$$T_{RB} \geq T_1 \quad (39)$$

Figure 2 summarizes the results of Equations (35) and (39) in a 'failure mode plot,' which represents the estimate error ε_0 versus the test statistic q (the notation q stands for either q_{RB} or q_1). The alert limit ℓ and detection thresholds T_{RB} and T_1 define the boundaries of the HMI areas in the upper left-hand quadrant (shadowed in gray for SS, in gray and dark gray for RB RAIM). Under H_1 , the probability of being in the HMI area is the integrity risk. As the fault magnitude varies, the mean of ε_0 and the non-centrality parameter of q describe a 'fault mode line' passing through the origin, with slope \bar{g}_{F1} . According to Equation (35), the worst-case slope is identical for RB and SS RAIM. Thus, the larger the HMI area is,

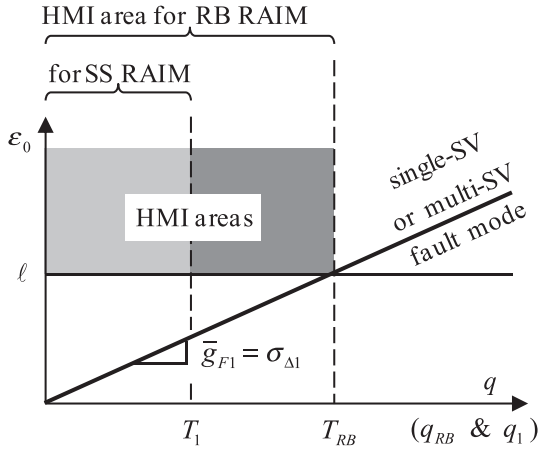


Fig. 2–Failure Mode Plot Illustrating the Comparison between RB and SS RAIM Assuming a Single Hypothesis H_1

the closer the failure mode line gets to the HMI area, and the higher the integrity risk becomes. It follows that the test statistic generating the lowest integrity risk is q_1 because its threshold T_1 is smaller than T_{RB} as indicated in Equation (39).

The difference between q_{RB} and q_1 can be interpreted as follows. It is apparent when substituting Equation (23) into (27) that the SS statistic q_1 is a function of the fault-free solution \hat{x}_1 under H_1 :

$$q_1 = (\hat{x}_0 - \hat{x}_1)/\sigma_{\Delta 1} \quad (40)$$

Therefore, under a simplifying single-hypothesis assumption, SS performs better than RB RAIM because, unlike q_{RB} , q_1 is tailored to the fault mode H_1 and to the state of interest x estimated by \hat{x}_0 and \hat{x}_1 . Thus, as illustrated in Figure 2, the two methods have identical failure mode slopes, but SS exploits knowledge of H_1 and x to reduce the impact of nominal noise, which is accounted for in the detection threshold.

In this section, a simplified single-hypothesis scenario was considered to perform a rigorous, analytical comparison of RB versus SS RAIM, thereby identifying fundamental differences between the two approaches. But, realistic integrity risk evaluation using Equation (2) requires the summing of terms over multiple hypotheses. The next section provides a graphical representation, which efficiently displays all fault hypotheses H_i , all test statistics q_{RB} and q_i , and also captures the correlation between q_i , for $i = 1, \dots, h$.

PARITY SPACE REPRESENTATIONS

The parity vector is the simplest, most fundamental expression of detection capability using measurement redundancy. Parity space representations have been introduced for RB RAIM by Potter and Suman in [3]. In this section, we exploit parity

space representations to analyze SS RAIM. First, we establish the relationships between the parity vector and the RB and SS test statistics, then RB and SS detection regions are displayed in parity space for a canonical example.

Parity Vector Definition and Relationship to RB RAIM

Both the RB and SS test statistics are derived from the $(n-m) \times 1$ parity vector \mathbf{p} , which lies in the $(n-m)$ -dimensional parity space, or left null space of \mathbf{H} , and can be expressed as [3, 4]:

$$\mathbf{p} \equiv \mathbf{Q}\mathbf{z} = \mathbf{Q}(\mathbf{v} + \mathbf{f}) \quad (41)$$

where the $(n-m) \times n$ parity matrix \mathbf{Q} is defined as:

$$\mathbf{Q}\mathbf{Q}^T = \mathbf{I}_{n-m} \text{ and } \mathbf{Q}\mathbf{H} = \mathbf{0}_{(n-m) \times m} \quad (42)$$

Equation (41) shows that \mathbf{p} is not a function of \mathbf{x} , and provides a scaled and noisy, direct observation of the fault vector \mathbf{f} , which needs to be detected. This is why \mathbf{p} is used as a basis for fault detection.

In addition, the measurement vector \mathbf{z} can be broken down into two orthogonal components respectively lying in the column space of \mathbf{H} and in the null space of \mathbf{H}^T : \mathbf{z} , and can be expressed as [3, 4]:

$$\mathbf{z} = \mathbf{H}\mathbf{S}_0\mathbf{z} + \mathbf{Q}^T\mathbf{Q}\mathbf{z} \quad (43)$$

Adding and subtracting $\mathbf{H}\mathbf{S}_0\mathbf{z}$ to \mathbf{z} , the measurement vector can be rewritten as:

$$\mathbf{z} = \mathbf{H}\mathbf{S}_0\mathbf{z} + (\mathbf{I}_n - \mathbf{H}\mathbf{S}_0)\mathbf{z} \quad (44)$$

By identification of the last term in Equations (43) and (44), we obtain:

$$\mathbf{Q}^T\mathbf{Q} = \mathbf{I}_n - \mathbf{H}\mathbf{S}_0. \quad (45)$$

As outlined in [3], substituting Equation (45) into (13), substituting the result into (14), and using the definitions in Equations (41) and (42) proves that the norms of \mathbf{p} and of the residual vector \mathbf{r} are equal:

$$q_{RB}^2 = \mathbf{r}^T\mathbf{r} = \mathbf{z}^T(\mathbf{I}_n - \mathbf{H}\mathbf{S}_0)\mathbf{z} = \mathbf{z}^T\mathbf{Q}^T\mathbf{Q}\mathbf{z} = \mathbf{p}^T\mathbf{p} \quad (46)$$

Equation (46) demonstrates the well-known result that RB RAIM is equivalent to ‘parity-based RAIM’ [4]. Parity-based RAIM is not further mentioned in this paper because it is identical to RB RAIM.

Solution Separations in Parity Space

As noted earlier, Appendix C shows that the test statistic q_i can be represented in parity space. However, the relationship between q_i and \mathbf{p} is not straightforward to establish because solution separations are defined in the position domain in Equations (23) and (27).

This issue is addressed for single-measurement faults, i.e., for $n_i = 1$, by first defining failure mode lines. The mean of random vector \mathbf{p} generated by a

fault on the i^{th} measurement, and expressed by substituting Equation (17) into (41), has a unit direction vector defined as:

$$\mathbf{u}_i \equiv \frac{\mathbf{Q}\mathbf{A}_i}{\sqrt{\mathbf{A}_i^T \mathbf{Q}^T \mathbf{Q} \mathbf{A}_i}} \text{ for } i = 1, \dots, n \quad (47)$$

where

$$\mathbf{A}_i^T = \begin{bmatrix} \mathbf{0}_{(i-1) \times 1}^T & 1 & \mathbf{0}_{(n-i) \times 1}^T \end{bmatrix} \quad (48)$$

i.e., \mathbf{A}_i is the matrix defined in Equation (18), but is restricted in Equations (47) and (48) to single-SV faults. Thus, $\mathbf{Q}\mathbf{A}_i$ is the i^{th} column of \mathbf{Q} . In parity space, the line passing through the origin with direction vector \mathbf{u}_i is the fault line corresponding to a fault on the i^{th} measurement.

Appendix G provides an analytical proof that for single-measurement faults ($n_i=1$), the n solution separations are projections of the parity vector on their corresponding fault mode lines.

$$q_i = \frac{s_{\Delta i}^T}{\sigma_{\Delta i}} \mathbf{z} = \mathbf{u}_i^T \mathbf{p} \quad (49)$$

To illustrate this result, we introduce a canonical example, which is then used in the rest of the paper.

Detection Regions for a Canonical Example

Let us consider a scalar state x and a 3×1 measurement vector \mathbf{z} defined as:

$$\mathbf{z} = \mathbf{H}x + \mathbf{v} + \mathbf{f} \quad (50)$$

where

$$\mathbf{H} = \begin{bmatrix} 1 & 1 & 1 \end{bmatrix}^T \text{ and } \mathbf{v} \sim N(\mathbf{0}_{3 \times 1}, \mathbf{I}_3) \quad (51)$$

Since $m=1$ and $n=3$, the $(n-m)$ parity space is two-dimensional, which is convenient for display. (This example is similar to the one used by Potter and Suman in [3].)

The fault vector \mathbf{f} represents three single-measurement faults, corresponding to three fault hypotheses H_i , with unknown fault magnitude f_i .

$$\mathbf{f} = \begin{bmatrix} f_1 \\ 0 \\ 0 \end{bmatrix} \text{ or } \mathbf{f} = \begin{bmatrix} 0 \\ f_2 \\ 0 \end{bmatrix} \text{ or } \mathbf{f} = \begin{bmatrix} 0 \\ 0 \\ f_3 \end{bmatrix} \quad (52)$$

As the fault magnitude f_i varies from $-\infty$ to $+\infty$, the mean parity vector describes a line in the parity space called the fault mode line, with direction vector \mathbf{u}_i defined in Equation (47).

Figure 3 illustrates Equations (46) and (49). The RB test statistic q_{RB} is the norm of the parity vector \mathbf{p} , whereas SS test statistics q_i , for $i=1, \dots, 3$, are orthogonal projections of \mathbf{p} onto each of the three fault mode lines. Vector \mathbf{p} is a bivariate normally distributed random vector, with unit-variance i.i.d. elements. In this two-dimensional parity space, a line of constant joint probability density describes a

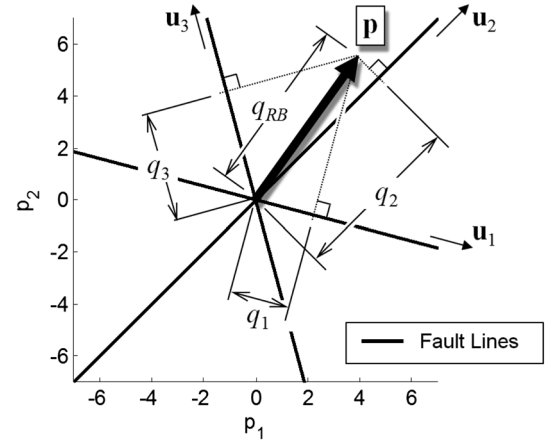


Fig. 3—Detection Test Statistics for RB (q_{RB}) and SS (q_1, q_2, q_3) in Parity Space

circle (not represented) centered at the origin under H_0 , and a circle centered along the i^{th} fault mode line given a fault hypothesis H_i .

In addition, for RB RAIM, the probability of no detection, which is the second term of the product in Equation (29), is given by: $P(q_{RB}^2 < T_{RB}^2 | H_i \cap \bar{\mathbf{f}}_i)$. In contrast, for SS RAIM, the probability of no detection is a joint probability that can be written as:

$$P(|q_1| < T_1 \cap |q_2| < T_2 \cap |q_3| < T_3 | H_i \cap \bar{\mathbf{f}}_i) \quad (53)$$

The correlation between test statistics q_i is represented in Figure 3 by the angles between the fault lines. Two perpendicular fault lines would correspond to uncorrelated test statistics, which are also jointly-Gaussian distributed, so that these variables would be statistically independent. This is not generally the case. For the canonical example, Figure 3 shows that the three SS test statistics q_i are correlated because the fault lines are not mutually orthogonal. Thus, unlike in Equation (29), Equation (53) cannot be written as the product of probabilities. The evaluation of the joint probability in Equation (53) is addressed in detail in the next section.

Finally, it follows from Equations (46), (49), and (53) that the detection boundaries for RB and SS RAIM are a circle (or a hyper-sphere in higher-dimensional parity space) and a polygon (or a hyper-polytope), respectively. If the SS detection thresholds are all equal ($T_1=T_2=T_3$), then the polygon is a hexagon. In Figure 4, detection is established if the parity vector \mathbf{p} lands outside the detection boundary. Therefore, the probability of no detection is the probability of being inside the dash-dotted circle for RB RAIM, and inside the hexagon for SS RAIM.

At this point, we have established that under the simplified single-hypothesis scenario, SS RAIM would perform better than RB RAIM. When taking multiple hypotheses into account, each method generates a different detection boundary, but it is unclear which one actually generates the smallest

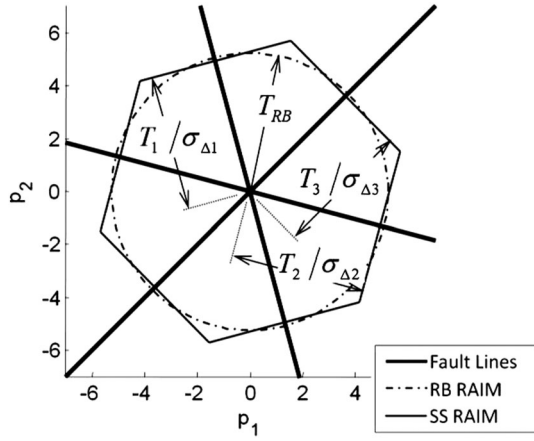


Fig. 4–Detection Boundaries for RB (Circle) and SS (Hexagon) in Parity Space

integrity risk. The following section provides a practical method to evaluate the integrity and continuity risks using RB and SS RAIM.

PRACTICAL APPROACH TO SOLUTION SEPARATION RAIM

Integrity and continuity risk evaluation using RB RAIM is achieved by respectively replacing $|q|$ and T with q_{RB}^2 and T_{RB}^2 in Equations (3) and (29), and then substituting (29) into (2). For SS RAIM, the inequalities (2) and (3) respectively become:

$$\sum_{i=0}^h P(|\varepsilon_0| > \ell \cap |\Delta_1| < T_{\Delta 1} \cap \dots \cap |\Delta_h| < T_{\Delta h} | H_0) P_{H_0} \quad (54)$$

$$\leq I_{REQ} - P_{> n_{MIN}}$$

$$P(|\Delta_1| \geq T_{\Delta 1} \cup \dots \cup |\Delta_h| \geq T_{\Delta h} | H_0) P_{H_0} \leq C_{REQ} \quad (55)$$

where the more conventional test statistic Δ_i is used instead of the equivalent normalized statistic q_i , which was expressed in Equation (27) as: $q_i = \Delta_i / \sigma_{\Delta i}$. In this case, the detection thresholds for Δ_i are defined as:

$$T_{\Delta i} = T_i \sigma_{\Delta i} \quad (56)$$

Direct evaluation of the joint probabilities in Equations (54) and (55) is cumbersome because the h test statistics Δ_i are correlated. Their joint probabilities could be computed using numerical procedures that involve the integration of multidimensional probability density functions (e.g., see [19]), but these procedures are computationally expensive, especially if $h \geq 4$. Therefore, in practical, real time implementations where processing resources are limited, the integrity and continuity risks are typically upper-bounded using a computationally-efficient approach. This section provides a step-by-step derivation of the integrity and continuity risk bounding method used in SS RAIM. The objective is to identify, explain, and illustrate the conservative assumptions ultimately

leading to protection level equations found in the literature in [5, 7].

Continuity Risk Allocation Using SS RAIM

The left-hand side of Equation (55) is the probability of false alarms or continuity risk. It can be upper-bounded as follows:

$$P(|\Delta_1| \geq T_{\Delta 1} \cup \dots \cup |\Delta_h| \geq T_{\Delta h} | H_0) P_{H_0} \quad (57)$$

$$\leq \sum_j^h P(|\Delta_j| \geq T_{\Delta j} | H_0) P_{H_0}$$

where subscript ‘j’ is used to index the SS test statistics. This continuity risk bound is interpreted in Figure 5 using a parity space representation for the canonical example introduced in the previous section. The left-hand side term in Equation (57) is the probability (to be over-bounded) of the parity vector \mathbf{p} being outside the white hexagon under H_0 . The same detection region is covered by the right-hand side sum of probabilities corresponding to all gray-shaded areas, but the probabilities of \mathbf{p} being in the medium-gray and dark-gray shaded areas are respectively double and triple-counted. Fortunately the probability of \mathbf{p} being in these medium and dark-gray areas is relatively small, as indicated by the lines of constant probability density. These contours describe concentric circles centered at the origin under H_0 , and are labeled in terms of $-\log_{10} f_{\mathbf{p}}(p_1, p_2)$, where $f_{\mathbf{p}}(p_1, p_2)$ is the probability density function of the bivariate normally distributed parity vector \mathbf{p} .

The continuity risk bound in Equation (57) allows the evaluation of the fault-free detection probabilities for each test statistic individually. This bound can be exploited to determine the values of the thresholds $T_{\Delta j}$ ensuring that the requirement

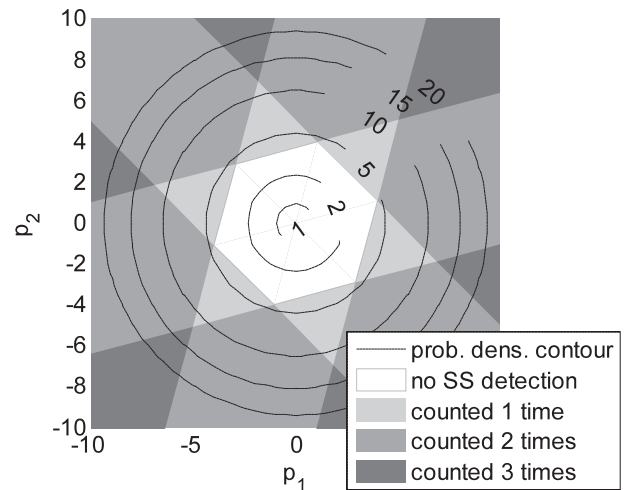


Fig. 5–Conservative Assumption in Continuity Risk Evaluation Using SS RAIM

C_{REQ} is satisfied. The SS detection thresholds can be computed using the following equations:

$$T_{\Delta j} = Q^{-1} \left\{ \frac{C_{REQj}}{2P_{H0}} \right\} \sigma_{\Delta j} \quad (58)$$

$$C_{REQ} = \sum_{j=1}^h C_{REQ,j}, \text{ e.g., } C_{REQ,j} = \frac{C_{REQ}}{h} \quad (59)$$

where the function $Q^{-1}\{\}$ is the inverse tail probability distribution of the two-tailed standard normal distribution ($Q\{\} = 1 - \Phi\{\}$, where $\Phi\{\}$ is the standard normal cumulative distribution function). For example, Equations (58) and (59) were used in Figures 4 and 5 to determine $T_{\Delta j}$ for $j=1, \dots, 3$ assuming $C_{REQ} = 10^{-6}$.

Arbitrary continuity risk allocation, e.g., using the equal allocation expressed in Equation (59), ensures that the continuity risk requirement is met, but can cause the integrity risk bound to be loose. In contrast, continuity risk allocation does not need to be addressed in RB RAIM where a single test statistic is used.

Integrity Risk Evaluation and Protection Level Derivation Using SS RAIM

The detection thresholds $T_{\Delta j}$ defined in Equation (58) can then be used to evaluate the integrity risk. In Equation (54), the integrity risk is expressed as a sum of probabilities over the fault-free hypothesis H_0 , and over faulted hypotheses H_i , for $i=1, \dots, h$.

First, under H_0 , a bound on the probability of HMI is established as follows:

$$\begin{aligned} P(|\varepsilon_0| > \ell, |\Delta_1| < T_{\Delta 1}, \dots, |\Delta_h| < T_{\Delta h} | H_0) \\ \leq P(|\varepsilon_0| > \ell | H_0) \end{aligned} \quad (60)$$

This bound is obtained by ignoring knowledge of no-detection. It can be considered a tight bound because, as illustrated in Figure 5, the probability of \mathbf{p} being in the white hexagon under H_0 is large. More precisely, Equations (58) and (59) guarantee that the probability of no false alarm stays larger than $1 - C_{REQ}$. Furthermore, the bound in Equation (60) is straightforward to evaluate because the distribution of ε_0 is fully defined (in Equation (21)) with zero mean under H_0 .

Second, in the presence of a fault, the integrity risk bound can be derived as follows:

$$\begin{aligned} P(|\varepsilon_0| > \ell, |\Delta_1| < T_{\Delta 1}, \dots, |\Delta_h| < T_{\Delta h} | H_i) \\ \leq P(|\varepsilon_0| > \ell, |\Delta_1| < T_{\Delta i} | H_i) \\ \leq P(|\varepsilon_0| > \ell | H_i, |\Delta_1| < T_{\Delta i}) P(|\Delta_1| < T_{\Delta i} | H_i) \\ \leq P(|\varepsilon_0| > \ell | H_i, |\Delta_1| < T_{\Delta i}) \end{aligned} \quad (61)$$

The first inequality in (61) ignores knowledge of no-detection for all test statistics, except for the one specifically designed to detect H_i (i.e., ignores knowledge of $|\Delta_j| < T_{\Delta j}, \forall j \neq i$). As illustrated in Figure 6, instead of limiting the no-detection region to the area inside the dashed hexagon, the bound considers the entire gray-shaded band. It is a tight bound because under H_i , the fault line is perpendicular to the gray band. The second inequality in Expression (61) is simply the conditional form of the previous line. It is worth noticing that, in contrast to Equation (29), a product of probabilities is derived from a joint probability without requiring that ε_0 be independent from the test statistic, i.e., without requiring that a least-squares estimator be implemented. The last inequality in (61) bounds $P(|\Delta_i| < T_{\Delta i} | H_i)$ with $P(|\Delta_i| < T_{\Delta i} | H_i) = 1$, which may result in a loose integrity risk bound: This point is further analyzed in the next section.

The convenience and efficiency of SS RAIM, which uses test statistics Δ_i directly derived in the position domain, is captured in the following inequality:

$$|\varepsilon_0| \leq |\varepsilon_i| + \underbrace{|\varepsilon_0 - \varepsilon_i|}_{|\Delta_i|} \quad (62)$$

The absolute values in Equation (62) capture the worst-case fault *direction* in the position domain. In addition, the worst-case fault *magnitude* is given by the condition ' $|\Delta_i| < T_{\Delta i}$ ' in expression (61). Thus, substituting the right-hand side of (62) into (61), applying the condition $|\Delta_i| < T_{\Delta i}$, and substituting the result into (54) provides the following integrity criterion:

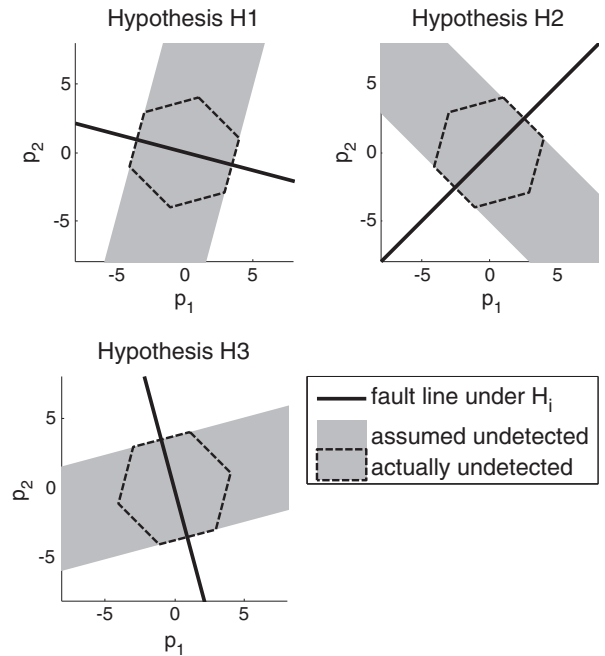


Fig. 6—Conservative Assumption in Integrity Risk Evaluation Using SS RAIM

$$\sum_{i=0}^h P(|\varepsilon_i| + T_{\Delta i} > \ell | H_i) P_{H_i} \leq I_{REQ} - P_{>n_{MIN}} \quad (63)$$

This expression is remarkable, because under H_i , ε_i is fault-free, and its zero-mean distribution is fully defined by Equation (22), without having to determine the worst-case fault vector $\bar{\mathbf{f}}_i$ in the measurement domain.

As an alternative to integrity risk evaluation, protection levels (PL) can be derived from Equation (63) [5, 7]. PLs are probability bounds on the position estimate error. They are used in practice because they provide an intuitive, spatial representation of the volume that is guaranteed to contain the true position with a probability higher than $1 - I_{REQ}$. A complete PL derivation can be found in [20] following the same steps as Equations (54) to (63) with the PL replacing the alert limit ℓ . PL generation requires one additional step to allocate I_{REQ} between the $h + 1$ terms of the sum in Equation (63). This step causes the PL-based integrity criterion to be more conservative than Equation (63), unless an allocation optimization process is carried out as outlined in [7]. This paper focuses on direct integrity risk evaluation rather than PL generation in order to maintain fair grounds for comparison with RB RAIM.

Practical Considerations When Comparing SS to RB RAIM

Major practical differences between RB and SS RAIM have emerged from the above derivation. On the one hand, SS RAIM requires that h detection test statistics (and h thresholds) be computed versus a single one for RB RAIM. Also, in SS RAIM, integrity risk evaluation is based on a series of conservative assumptions, whereas in RB RAIM, the integrity risk can directly be quantified using Equations (2), (3) and (29). On the other hand, direct integrity risk evaluation using RB RAIM is greatly facilitated using a least-squares estimator (to establish Equation (29)), which is not needed in SS RAIM. And, unlike RB RAIM, SS RAIM does not require that the worst-case directions for multi-SV faults be determined, nor does it require a search through fault magnitudes to find the worst-case fault vector.

In parallel, it is worth noting that, similar to PL generation in SS RAIM, variants of RB RAIM are often used in practice. In the most common implementation, rather than considering all fault hypotheses H_i , for $i = 1, \dots, h$ in Equation (2), one can identify the ‘worst-case’ fault hypothesis H_{WORST} , which maximizes the probability of HMI given H_i . In this case, the prior probability of the single fault hypothesis H_{WORST} is conservatively assumed to be: $\sum_{i=1}^h P_{H_i}$. Hypothesis H_{WORST} is straightforward to

find using RB RAIM, because it is the one for which the failure mode slope \bar{g}_{Fi} is the largest (\bar{g}_{Fi} is already computed in RB RAIM). This computationally-efficient upper bound on the RB RAIM integrity risk, which is a looser bound than the one previously described in Equations (2), (3) and (29), is sometimes referred to as ‘slope-based RAIM’ [7]. It is not pursued here, to preserve fair grounds for comparison between RB and SS RAIM.

Finally, other application-specific considerations can steer the design of an integrity monitoring algorithm towards either SS RAIM or RB RAIM. For example, the RB method is better suited for sequential RAIM implementations in [12], whereas SS provides a practical framework for estimator optimization in [21].

The next section presents a performance comparison to determine which of the two methods generates the lowest integrity risk, and under what circumstances.

PERFORMANCE COMPARISON

This section aims at analyzing the tightness of the SS integrity risk bound derived for practical applications, for varying values of the navigation requirements. The integrity risk bound is then used as a performance measure for comparison between RB and SS RAIM. The two algorithms are evaluated, first for the canonical example, and then, for a more realistic aircraft navigation application using multi-constellation Advanced RAIM (ARAIM).

Performance Evaluation for the Canonical Example

In the following paragraphs, the integrity risk bounds for RB and SS RAIM are first analyzed using the canonical example described in Equations (50) to (52), under single-measurement fault hypotheses. They are plotted in Figure 7 assuming a continuity risk requirement C_{REQ} of 10^{-6} and a prior probability

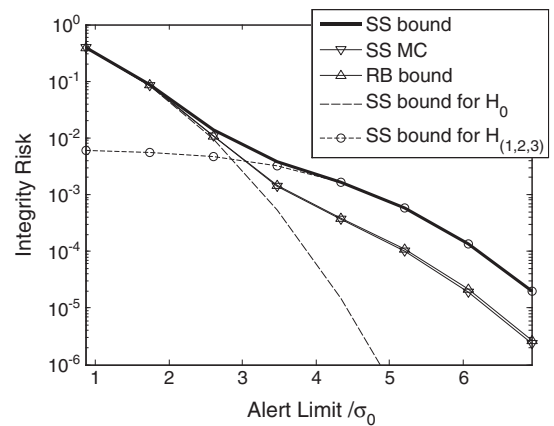


Fig. 7—Tightness of the Integrity Risk Bound using SS RAIM and Comparison with RB RAIM for the Canonical Example

of fault P_{H_i} of 10^{-3} , for $i = 1, \dots, 3$. The x-axis in Figure 7 presents values the non-dimensional parameter ℓ/σ_0 ranging from 1 to 7.

For SS RAIM, the requirement C_{REQ} is equally allocated among the three test statistics Δ_i following Equation (59). In this case, equal allocation is the optimal allocation because, as illustrated with the regularly separated fault lines in Figure 4, the three statistics Δ_i contribute equally to the integrity risk. The integrity risk bound for SS RAIM is plotted in Figure 7 with a thick, solid black line. To better understand this curve, the integrity risk in Equation (54) is broken down into two terms. The first term, corresponding to the fault-free hypothesis H_0 , is displayed in Figure 7 with a dashed curve, and is the dominating term in the total integrity risk bound for $\ell/\sigma_0 \leq 2.5$. The second term, representing the sum of probabilities over all fault hypotheses H_i , $i \neq 0$ (dotted curve in Figure 7), provides the largest contribution to the probability of HMI for $\ell/\sigma_0 \geq 3$.

In addition, for SS RAIM, the integrity risk bound derived for practical applications in Equation (63) (thick black line in Figure 7), is compared to the initial joint probability in Equation (54), still for SS RAIM but without the conservative assumptions. This joint probability is evaluated using a Monte Carlo simulation over 10^6 trials, and identified in Figure 7 with downward-pointing triangle markers. (It is worth noting that evaluating this joint probability requires that the worst case fault vector be determined, which is not needed in SS RAIM for the practical bound.) The two SS curves match for $\ell/\sigma_0 \leq 2.5$ (as long as the H_0 -term is dominating), but diverge for $\ell/\sigma_0 \geq 3$, reaching an order of magnitude difference for $\ell/\sigma_0 = 7$. This shows that the bounds on the probability of HMI are tight given H_0 , but are much looser under fault hypotheses H_i , $i \neq 0$. More precisely, as was pointed out in the previous section, in the last step of expression (59), bounding $P(|\Delta_i| < T_{\Delta_i} | H_i)$ with $P(|\Delta_i| < T_{\Delta_i} | H_i) = 1$ could produce a loose bound, which is the price to pay to enable integrity risk evaluation without real-time Monte-Carlo trials or integration of multivariate probability density functions.

Finally, SS RAIM is compared with RB RAIM, for which upward-pointing triangle markers designate the integrity risk bound in Figure 7. The RB curve matches the SS curve established using the Monte-Carlo simulation, i.e., evaluated without the assumptions needed to obtain the analytical bound for SS RAIM. The RB curve is actually slightly above the curve labeled 'SS MC' (for SS Monte Carlo) and this difference is caused by the circular versus hexagonal detection regions in Figure 4. In this canonical example, for large values of the non-dimensional parameter ℓ/σ_0 , the integrity risk bound using RB RAIM is an order of magnitude lower than the SS bound derived for practical implementations.

The sensitivity of the integrity risk bounds for RB and SS RAIM is further analyzed in Figure 8, where both the non-dimensional parameter ℓ/σ_0 and the continuity risk requirement C_{REQ} are varied for the canonical example. It shows again an order of magnitude difference between the two bounds when ℓ/σ_0 is larger than five. This trend is further accentuated for large values of C_{REQ} , in the lower right-hand corner of Figure 8. In order to check whether this difference between RB and SS RAIM is still significant in a more realistic example, the integrity risk bounds are evaluated for a benchmark aviation navigation application.

Benchmark Aircraft Navigation Application

This section presents a performance evaluation of RB versus SS Advanced RAIM (ARAIM) for vertical guidance of aircraft using dual-frequency GPS and Galileo. The simulation parameters, which include ARAIM measurement errors, and LPV-200 navigation requirements (to support localizer precision vertical aircraft approach operations down to 200 feet above the ground), are listed in Table 1 and described in detail in [9]. In Table 1, one major difference with the ARAIM error model in [9] is that fault-free measurement biases, labeled b_{MAX} , are assumed to be zero. These biases introduce application-specific complications whose treatment is not relevant to this paper. The alert limit ℓ is also reduced from 35 m in ARAIM to 10 m in this paper. A '24-1' GPS satellite constellation and a '27-1' Galileo constellations are assumed, which are nominal constellations with one spacecraft removed to account for outages; these example constellations are also described in [9]. The integrity risk evaluation procedure described at the beginning of this paper is implemented. Integrity risk contributions are evaluated for single-SV faults, as well as for dual-SV faults if their prior probability

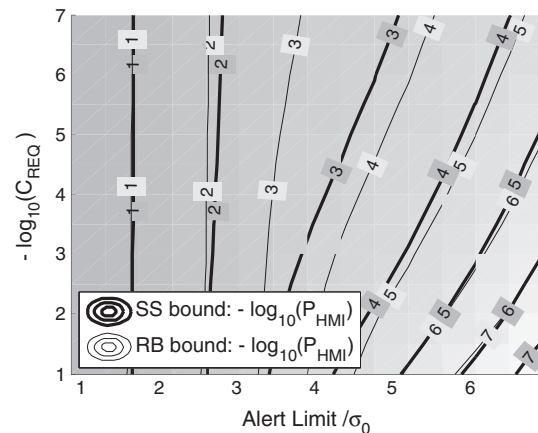


Fig. 8—Comparison between RB and SS Integrity Risk Bounds Versus Alert Limit and Continuity Risk Requirement (C_{REQ}) for the Canonical Example

Table 1—Simulation Parameters

Description	Value
SV clock and orbit error (URA)	0.75 m (0.957 m for Galileo)
Residual tropospheric error *	$0.12 \frac{1.001}{(0.002001 + \sin^2 \xi)^{1/2}}$ m
Smoothed code multipath *	$0.13 + 0.53e^{-\xi/10}$ m (lookup table for Galileo [9])
Smoothed code receiver noise *	$0.15 + 0.43e^{-\xi/6.9}$ m
Fault-free ranging bias b_{MAX}	0 m
Integrity risk requirement I_{REQ}	10^{-7}
Continuity risk requirement C_{REQ}	$2 \cdot 10^{-6}$
Prior probability of satellite fault P_{Hi}	10^{-5}
Prior probability of constellation fault	none considered

* : ξ is the satellite elevation angle in degrees.

of occurrence exceeds 10^{-8} , which is the case using the joint GPS/Galileo system when the number of satellites is larger than 15. Moreover, this analysis focuses on the vertical position coordinate, for which the aircraft approach navigation requirements are often the most difficult to fulfill.

In Figure 9, integrity risk bounds are evaluated over 24 hours at an example Chicago location. The bounds for RB and SS RAIM are respectively displayed with dotted and solid curves. The thick curves were established using GPS only, and are mostly above the integrity risk requirement I_{REQ} (indicated by a dashed horizontal line). In contrast, the thin curves assuming SV signals from GPS and Galileo are mostly below I_{REQ} , which illustrates the performance impact of augmenting GPS with redundant Galileo measurements. The solid curves are both above their corresponding dotted curves confirming the observation made for the canonical example that the SS integrity risk bound is looser

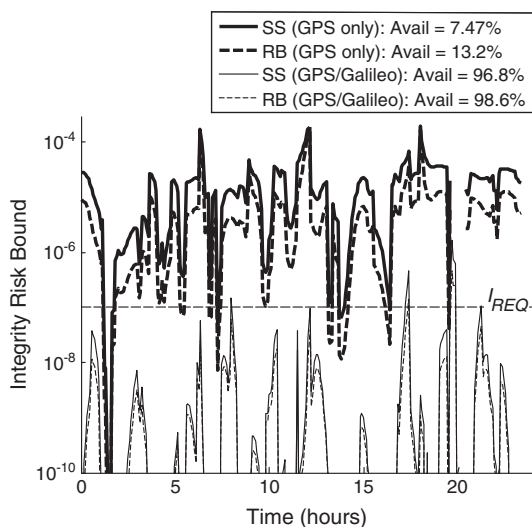


Fig. 9—Integrity Risk Bound Evaluation Using RB Versus SS RAIM for Multi-Constellation ARAIM Over 24 Hours at Chicago Location

than the RB bound. This difference is quantified by computing availability, which is the fraction of time where the curves are below I_{REQ} over 24 hours. Availability increases from 7.5% for SS RAIM to 13.2% for RB RAIM using GPS only, and from 96.8% to 98.6% using GPS / Galileo. Depending on the application, this improvement can be substantial, but it comes at the cost of higher computation time to determine the worst case fault magnitude in RB RAIM.

CONCLUSION

This paper provides a step-by-step derivation of residual-based (RB) and solution separation (SS) RAIM for the detection of single and multi-measurement faults that are likely to occur in future multi-constellation GNSS.

An analytical comparison between SS and RB RAIM is carried out based on a derivation of the worst-case measurement fault vector, which maximizes the integrity risk in the presence of multiple simultaneous faults. The paper shows that the SS detection test statistics are tailored to the fault hypotheses and to the state of interest, and could thereby, in theory (i.e., under a simplifying single-hypothesis assumption), reduce the integrity risk as compared to RB RAIM. However, in practice, conservative assumptions are required in SS RAIM to evaluate integrity risk. These conservative assumptions, not needed in RB RAIM, outweigh the theoretical advantage of SS over RB RAIM. To support this analysis, a parity-space representation is developed for single-satellite faults, describing the RB and SS detection boundaries in parity space as a hyper-sphere and a polytope, respectively.

An example Advanced RAIM (ARAIM) application for aircraft approach navigation using ranging signals from GPS and Galileo satellites was implemented to quantify the performance improvement of RB RAIM versus SS RAIM. With regard to processing efficiency, RB RAIM uses a single test statistic, whereas SS RAIM computes as many test statistics and detection thresholds as fault hypotheses. But, unlike in RB RAIM, the conservative assumptions made in SS RAIM eliminate the need to determine the worst-case measurement fault vector for each hypothesis.

Ultimately, the choice between the two methods should be made depending on the application, by determining whether the performance improvement brought by RB over SS RAIM is worth the increased computational load.

ACKNOWLEDGMENT

The authors would like to acknowledge Dr. Young. C. Lee for his careful review, and his precious and insightful comments on this paper.

APPENDIX A: MULTIPLE-HYPOTHESIS INTEGRITY RISK EVALUATION FOR MULTI-CONSTELLATION GNSS

The integrity risk P_{HMI} can be expressed considering a set of mutually exclusive, jointly exhaustive hypotheses. If n is the number of satellites in view, then the total number of hypotheses is 2^n , which includes all combinations of fault-free and faulted measurements. Fortunately, assuming independent faults across satellites, most of the fault combinations are extremely unlikely to occur, and do not need to be detected in order to meet a typical integrity risk requirement I_{REQ} (specified in [9] for an example application of aircraft approach navigation).

Let n_{MIN} be the minimum number of simultaneously faulted satellites which must be monitored against. Fault hypotheses can be separated into two groups, to distinguish combinations of more than n_{MIN} faulty measurements (labeled ' $> n_{MIN}$ '), from all other faults (' $\leq n_{MIN}$ '). The integrity risk can then be written using the law of total probability as:

$$P_{HMI} = P(HMI | \leq n_{MIN})P_{\leq n_{MIN}} + P(HMI | > n_{MIN})P_{> n_{MIN}} \quad (A-1)$$

The number n_{MIN} is determined such that the prior probability $P_{> n_{MIN}}$ is much smaller than I_{REQ} . $P_{> n_{MIN}}$ is given by:

$$P_{> n_{MIN}} = \sum_{k=n_{MIN}+1}^n C_k^n P_{sat}^k (1 - P_{sat})^{n-k} \quad (A-2)$$

where C_k^n is the binomial coefficient, and P_{sat} is the prior probability of individual satellite fault. It follows that in Equation (A-1), the term $P(HMI | > n_{MIN})$ can be upper bounded by $P(HMI | > n_{MIN}) = 1$. Since $P_{> n_{MIN}} \ll I_{REQ}$, the resulting bound on $P(HMI)$ is a tight integrity risk bound.

In Equation (A-1), the event ' $\leq n_{MIN}$ ' represents a number of individual hypotheses of $h+1$, where $h = \sum_{k=1}^{n_{MIN}} C_k^n$. Let H_0 be the fault-free hypothesis, and H_i , for $i=1, 2, \dots, h$, be the fault hypotheses. With these notations, and considering $P(HMI | > n_{MIN}) = 1$, the integrity criterion (Equation (2) in the text) can be expressed as:

$$\sum_{i=0}^h P(HMI | H_i) P(H_i) + P_{> n_{MIN}} < I_{REQ} \quad (A-3)$$

For example, assuming a P_{sat} of 10^{-4} and a number of visible satellites $n=10$, the prior probabilities of a single-SV fault P_{1F} , of dual-SV faults P_{2F} , and of three or more simultaneous faults $P_{>2F}$ are $1.0 \cdot 10^{-3}$, $4.5 \cdot 10^{-7}$, and $1.2 \cdot 10^{-10}$, respectively. For an example integrity risk requirement I_{REQ} of 10^{-7} , which is applicable to aircraft vertical guidance

[9, 10], P_{1F} and P_{2F} are both above I_{REQ} . The same remains true for larger values of n . This example illustrates that for multi-constellation GNSS where n is often larger than 10, it is not only crucial to detect cases of single SV faults, but also cases of two simultaneous faults. In contrast, $P_{>2F}$ remains at least two orders of magnitude below I_{REQ} , even as n increases to 20. Therefore, in this example, $n_{MIN}=2$.

APPENDIX B: COVARIANCE MATRIX OF THE SOLUTION SEPARATION VECTOR

This appendix shows that: $\mathbf{P}_{\Delta i} = \mathbf{P}_i - \mathbf{P}_0$. Let $E\{\}$ be the expected-value operator. The solution separation covariance matrix is defined as:

$$\mathbf{P}_{\Delta i} \equiv E\left\{(\mathbf{S}_0 - \mathbf{S}_i)\mathbf{v}\mathbf{v}^T(\mathbf{S}_0 - \mathbf{S}_i)^T\right\} \quad (B-1)$$

Under the assumption expressed in Equation (5) that $E\{\mathbf{v}\mathbf{v}^T\} = \mathbf{I}_n$, Equation (B-1) becomes:

$$\mathbf{P}_{\Delta i} = \mathbf{S}_0\mathbf{S}_0^T - \mathbf{S}_0\mathbf{S}_i^T - \mathbf{S}_i\mathbf{S}_0^T + \mathbf{S}_i\mathbf{S}_i^T \quad (B-2)$$

The second term in Equation (B-2) can be written, using the partitioning of Equations (17) and (18), as:

$$\begin{aligned} \mathbf{S}_0\mathbf{S}_i^T &= [\mathbf{P}_0\mathbf{H}^T\mathbf{A}_i \quad \mathbf{P}_0\mathbf{H}^T\mathbf{B}_i] \begin{bmatrix} \mathbf{0}_{n_i \times (n-n_i)} \\ \mathbf{I}_{n-n_i} \end{bmatrix} \mathbf{B}_i^T\mathbf{H}\mathbf{P}_i \\ &= \mathbf{P}_0\mathbf{H}^T\mathbf{B}_i\mathbf{B}_i^T\mathbf{H}\mathbf{P}_i = \mathbf{P}_0 \end{aligned} \quad (B-3)$$

Similarly, the third term in Equation (B-2) becomes:

$$\mathbf{S}_i\mathbf{S}_0^T = \mathbf{P}_0 \quad (B-4)$$

Finally, substituting Equations (B-3) and (B-4) into (B-2), and noticing that the first and last terms in Equation (B-2) are respectively equal to \mathbf{P}_0 and \mathbf{P}_i (by definition of \mathbf{S}_0 and \mathbf{S}_i in Equations (10) and (20)) gives the following equation:

$$\mathbf{P}_{\Delta i} = \mathbf{P}_0 - \mathbf{P}_0 - \mathbf{P}_0 + \mathbf{P}_i \quad (B-5)$$

which establishes the proof.

APPENDIX C: INDEPENDENCE OF LEAST-SQUARES ESTIMATE ERRORS FROM RB AND SS TEST STATISTICS

This appendix proves the independence of the least squares estimate error ϵ_0 with any test statistic derived in parity space, which includes the RB test statistic q_{RB} and the SS test statistics Δ_i (or equivalently q_i), for $i=1, \dots, h$.

Let \mathbf{D} be an $n_D \times n$ matrix used to generate an $n_D \times 1$ detector vector (or scalar) $\mathbf{D}\mathbf{z}$ from which the

test statistic is derived. For example, the following detectors are defined in the text:

$$\text{for RB RAIM : } n_D = n, \mathbf{D} = \mathbf{I}_n - \mathbf{H}\mathbf{S}_0 \text{ and } \mathbf{D}\mathbf{z} = \mathbf{r} \quad (\text{C-1})$$

$$\text{for SS RAIM : } n_D = 1, \mathbf{D} = \mathbf{s}_{\Delta i}^T (\mathbf{S}_0 - \mathbf{S}_i) \text{ and } \mathbf{D}\mathbf{z} = \Delta_i \quad (\text{C-2})$$

An effective detector $\mathbf{D}\mathbf{z}$ provides a direct observation of the fault vector \mathbf{f} in Equation (4). Therefore, $\mathbf{D}\mathbf{z}$ cannot be a function of \mathbf{x} , which is expressed as:

$$\mathbf{D}\mathbf{H} = \mathbf{0}. \quad (\text{C-3})$$

Equation (C-3) expresses the fact that matrix \mathbf{D} maps the measurement vector into the parity space (or null space of \mathbf{H}^T). The correlation between ε_0 and $\mathbf{D}\mathbf{z}$ is given by:

$$\mathbb{E}\{(\mathbf{D}\mathbf{z})\varepsilon_0^T\} = \mathbb{E}\{\mathbf{D}\mathbf{v}\mathbf{v}^T\mathbf{s}_0\} = \mathbf{D}\mathbf{s}_0 = \mathbf{D}\mathbf{H}\mathbf{P}_0\mathbf{a} = \mathbf{0} \quad (\text{C-4})$$

where Equation (C-3) was used, and for clarity of exposition, mean errors caused by \mathbf{f} were implicitly removed.

Equation (C-4) shows that the least-squares estimate error ε_0 is uncorrelated with any vector $\mathbf{D}\mathbf{z}$ lying in parity space. Vector $\mathbf{D}\mathbf{z}$ and ε_0 are also jointly normally distributed. Therefore, all elements of $\mathbf{D}\mathbf{z}$ are linearly independent from ε_0 , which ensures that any combination of these elements (including the norm q_{RB} of $\mathbf{D}\mathbf{z} = \mathbf{r}$ for RB RAIM) is statistically independent from the estimate error ε_0 .

It is straightforward to show that Equation (C-3) is satisfied for both RB and SS RAIM (because $\mathbf{S}_0\mathbf{H} = \mathbf{I}$ and $\mathbf{S}_i\mathbf{H} = \mathbf{I}$). Thus, both q_{RB} and Δ_i (or equivalently q_i) are derived from a vector lying in parity space, and, according to Equation (C-4), are statistically independent from ε_0 .

APPENDIX D: WORST-CASE FAULT DIRECTION DERIVATION FOR RB AND SS RAIM

This appendix provides a derivation of the worst-case fault vector direction $\bar{\mathbf{f}}_i$, which maximizes the integrity risk under hypothesis H_i . In this appendix, $\bar{\mathbf{f}}_i$ designates the worst-case fault direction, the worst-case fault magnitude being treated separately using a straightforward search routine as described in the text.

Under H_i , the $n_i \times 1$ vector \mathbf{f}_{Ai} of non-zero elements of the $n \times 1$ fault vector \mathbf{f} is defined as:

$$\mathbf{f}_{Ai} \equiv \mathbf{A}_i^T \mathbf{f}, \text{ i.e., } \mathbf{f} = \mathbf{A}_i \mathbf{f}_{Ai} \quad (\text{D-1})$$

It is worth noticing for upcoming derivations, that:

$$\begin{aligned} \mathbf{B}_i^T \mathbf{A}_i &= \mathbf{0}_{(n-n_i) \times n_i} \text{ hence, } \mathbf{s}_i^T \mathbf{A}_i = \mathbf{0}_{1 \times n_i} \\ \text{and } \mathbf{s}_{\Delta i}^T \mathbf{A}_i &= \mathbf{s}_0^T \mathbf{A}_i \end{aligned} \quad (\text{D-2})$$

which is obvious from the definitions of \mathbf{A}_i , \mathbf{B}_i , \mathbf{s}_i , and $\mathbf{s}_{\Delta i}$ in Equations (18), (20), and, (25).

For SS RAIM, substituting Equation (D-1) into (30), and substituting (D-2) into the resulting expression shows that [18]:

$$g_{Fi}^2 \equiv \frac{\mathbf{f}_{Ai}^T \mathbf{A}_i^T \mathbf{s}_0 \mathbf{s}_0^T \mathbf{A}_i \mathbf{f}_{Ai}}{\mathbf{f}_{Ai}^T \mathbf{A}_i^T \mathbf{s}_{\Delta i} \mathbf{s}_{\Delta i}^T \mathbf{A}_i \mathbf{f}_{Ai}} \sigma_{\Delta i}^2 = \sigma_{\Delta i}^2 \quad (\text{D-3})$$

This result is independent of fault direction. Thus, for SS RAIM, the worst-case fault slope squared, noted \bar{g}_{Fi}^2 , is $\sigma_{\Delta i}^2$.

In addition, for RB RAIM, substituting Equation (D-1) into (30) and using the following change of variables:

$$\mathbf{f}_{Ai} = \mathbf{M}_{Ai} \mathbf{f}_{Ai}^* \quad (\text{D-4})$$

Equation (30) becomes

$$g_{Fi}^2 = \frac{\mathbf{f}_{Ai}^{*T} \mathbf{M}_{Ai}^T \mathbf{m}_{Xi} \mathbf{m}_{Xi}^T \mathbf{M}_{Ai} \mathbf{f}_{Ai}^*}{\mathbf{f}_{Ai}^{*T} \mathbf{f}_{Ai}^*} \quad (\text{D-5})$$

where,

$$\begin{aligned} \mathbf{m}_{Xi} &= \mathbf{A}_i^T \mathbf{s}_0 \\ \mathbf{M}_{Ai} &= (\mathbf{A}_i^T (\mathbf{I}_n - \mathbf{H}\mathbf{S}_0) \mathbf{A}_i)^{-1/2} \end{aligned}$$

It follows from Equation (D-5) that the worst-case fault slope squared \bar{g}_{Fi}^2 under H_i is the maximum eigenvalue of the $n_i \times n_i$ matrix [11, 12]:

$$\mathbf{M}_{Ai}^T \mathbf{m}_{Xi} \mathbf{m}_{Xi}^T \mathbf{M}_{Ai} \quad (\text{D-6})$$

and the corresponding eigenvector \mathbf{v}_{MAXi} can be used to express the worst-case fault direction $\bar{\mathbf{f}}_i$ under H_i as:

$$\bar{\mathbf{f}}_i = \mathbf{A}_i \mathbf{M}_{Ai} \mathbf{v}_{MAXi} \quad (\text{D-7})$$

The expression of $\bar{\mathbf{f}}_i$ in terms of vector \mathbf{v}_{MAXi} , which is numerically determined, does not allow us to establish analytical proofs when comparing RB and SS RAIM in the next section. Instead, a fully analytical expression of $\bar{\mathbf{f}}_i$ is sought, for example, in terms of \mathbf{A}_i , \mathbf{M}_{Ai} and \mathbf{m}_{Xi} . To find this expression, let matrix \mathbf{M} be defined as:

$$\mathbf{M} \equiv \mathbf{M}_{Ai}^T \mathbf{m}_{Xi} (\mathbf{m}_{Xi}^T \mathbf{M}_{Ai} \mathbf{M}_{Ai}^T \mathbf{m}_{Xi})^{-1} \mathbf{m}_{Xi}^T \mathbf{M}_{Ai} \quad (\text{D-8})$$

\mathbf{M} is the $n_i \times n_i$ matrix in Equation (D-6) multiplied by the scalar ‘normalizing factor’ $(\mathbf{m}_{Xi}^T \mathbf{M}_{Ai} \mathbf{M}_{Ai}^T \mathbf{m}_{Xi})^{-1}$. It can easily be shown that \mathbf{M} is symmetric and idempotent:

$$\mathbf{M} = \mathbf{M}^T \text{ and } \mathbf{M} = \mathbf{M}\mathbf{M} \quad (\text{D-9})$$

Matrix \mathbf{M} is called an orthogonal projector and is derived from an outer product (because $\mathbf{M}_{Ai}^T \mathbf{m}_{Xi}$ in Equation (D-8) is an $n_i \times 1$ vector). Therefore, \mathbf{M} has a single non-zero eigenvalue, of value 1. It follows that the matrix in Equation (D-6) has a single non-zero eigenvalue, with value equal to the inverse of

the normalizing factor used in Equation (D-8). This provides an expression of the worst-case failure mode slope \bar{g}_{Fi} :

$$\bar{g}_{Fi}^2 = \mathbf{m}_{Xi}^T \mathbf{M}_{Ai} \mathbf{M}_{Ai}^T \mathbf{m}_{Xi} \quad (\text{D-10})$$

In addition, substituting \bar{g}_{Fi}^2 for g_{Fi}^2 in Equation (D-8) and solving by inspection for \mathbf{f}_{Ai}^* shows that the direction of \mathbf{f}_{Ai}^* that maximizes g_{Fi}^2 is aligned with vector $\mathbf{M}_{Ai}^T \mathbf{m}_{Xi}$. Thus, the conclusion of this appendix is that the worst-case fault direction $\bar{\mathbf{f}}_i$ under a multi-measurement fault hypothesis H_i can be expressed analytically in a compact form as:

$$\bar{\mathbf{f}}_i = \mathbf{A}_i \mathbf{M}_{Ai} \mathbf{M}_{Ai}^T \mathbf{m}_{Xi} \quad (\text{D-11})$$

i.e.,

$$\bar{\mathbf{f}}_i = \mathbf{A}_i (\mathbf{A}_i^T (\mathbf{I}_n - \mathbf{H}\mathbf{S}_0) \mathbf{A}_i)^{-1} \mathbf{A}_i^T \mathbf{s}_0 \quad (\text{D-12})$$

APPENDIX E: ANALYTICAL COMPARISON OF RB AND SS RAIM TEST STATISTICS

This appendix proves that $q_{RB} = q_i$ if and only if $n_i = n - m = 1$.

First, by substituting into Equation (10) the definition of the partitioned matrix \mathbf{H} given in Equation (17), the following result is established:

$$\mathbf{P}_0^{-1} = \mathbf{H}^T \mathbf{H} = \mathbf{H}^T \mathbf{A}_i \mathbf{A}_i^T \mathbf{H} + \mathbf{H}^T \mathbf{B}_i \mathbf{B}_i^T \mathbf{H} \quad (\text{E-1})$$

hence, using the definition of \mathbf{P}_i in Equation (20):

$$\mathbf{P}_i^{-1} = \mathbf{H}^T \mathbf{B}_i \mathbf{B}_i^T \mathbf{H} = \mathbf{P}_0^{-1} - \mathbf{H}^T \mathbf{A}_i \mathbf{A}_i^T \mathbf{H} \quad (\text{E-2})$$

The definition of the variance of the fault-free subset solution in Equation (18) becomes:

$$\sigma_i^2 = \boldsymbol{\alpha}^T \mathbf{P}_i \boldsymbol{\alpha} = \boldsymbol{\alpha}^T (\mathbf{P}_0^{-1} - \mathbf{H}^T \mathbf{A}_i \mathbf{A}_i^T \mathbf{H})^{-1} \boldsymbol{\alpha} \quad (\text{E-3})$$

Using the matrix inversion lemma, Equation (E-3) becomes:

$$\begin{aligned} \sigma_i^2 &= \boldsymbol{\alpha}^T \left(\mathbf{P}_0 + \mathbf{P}_0 \mathbf{H}^T \mathbf{A}_i (\mathbf{I}_{n_i} - \mathbf{A}_i^T \mathbf{H} \mathbf{P}_0 \mathbf{H}^T \mathbf{A}_i)^{-1} \mathbf{A}_i^T \mathbf{H} \mathbf{P}_0 \right) \boldsymbol{\alpha} \\ &= \sigma_0^2 + \boldsymbol{\alpha}^T \mathbf{S}_0 \mathbf{A}_i (\mathbf{A}_i^T \mathbf{A}_i - \mathbf{A}_i^T \mathbf{H} \mathbf{S}_0 \mathbf{A}_i)^{-1} \mathbf{A}_i^T \mathbf{S}_0^T \boldsymbol{\alpha} \\ &= \sigma_0^2 + \mathbf{s}_0^T \mathbf{A}_i (\mathbf{A}_i^T (\mathbf{I}_n - \mathbf{H}\mathbf{S}_0) \mathbf{A}_i)^{-1} \mathbf{A}_i^T \mathbf{s}_0 \end{aligned} \quad (\text{E-4})$$

Using the result of APPENDIX B, the variance of the single-state solution separation can then be expressed as:

$$\sigma_{\Delta i}^2 = \sigma_i^2 - \sigma_0^2 = \mathbf{s}_0^T \mathbf{A}_i (\mathbf{A}_i^T (\mathbf{I}_n - \mathbf{H}\mathbf{S}_0) \mathbf{A}_i)^{-1} \mathbf{A}_i^T \mathbf{s}_0 \quad (\text{E-5})$$

Pre-multiplying both sides by $\mathbf{A}_i^T \mathbf{s}_0$ and post-multiplying by $\mathbf{s}_0^T \mathbf{A}_i$ yields:

$$\sigma_{\Delta i}^2 \mathbf{A}_i^T \mathbf{s}_0 \mathbf{s}_0^T \mathbf{A}_i = \mathbf{A}_i^T \mathbf{s}_0 \mathbf{s}_0^T \mathbf{A}_i (\mathbf{A}_i^T (\mathbf{I}_n - \mathbf{H}\mathbf{S}_0) \mathbf{A}_i)^{-1} \mathbf{A}_i^T \mathbf{s}_0 \mathbf{s}_0^T \mathbf{A}_i \quad (\text{E-6})$$

Since \mathbf{A}_i is an $n \times n_i$ matrix, if $n_i = 1$, then $\mathbf{A}_i^T \mathbf{s}_0 \mathbf{s}_0^T \mathbf{A}_i$ is a non-zero scalar. Multiplying both sides of the previous equation by the inverse squared of this scalar and taking the inverse of the resulting expression gives the following equation:

$$\mathbf{A}_i^T \mathbf{s}_0 \mathbf{s}_0^T \mathbf{A}_i / \sigma_{\Delta i}^2 = \mathbf{A}_i^T (\mathbf{I}_n - \mathbf{H}\mathbf{S}_0) \mathbf{A}_i \quad (\text{E-7})$$

In parallel, substituting the partitioned expressions of \mathbf{f} in Equations (17) and (D-1) into the definitions of λ_{RB}^2 and λ_i^2 in Equations (16) and (28), the non-centrality parameters λ_{RB}^2 and λ_i^2 of q_{RB} and q_i can respectively be expressed as:

$$\lambda_{RB}^2 = \mathbf{f}_{Ai}^T \mathbf{A}_i^T (\mathbf{I}_n - \mathbf{H}\mathbf{S}_0) \mathbf{A}_i \mathbf{f}_{Ai} \quad (\text{E-8})$$

$$\lambda_i^2 = \mathbf{f}_{Ai}^T \mathbf{A}_i^T \mathbf{s}_0 \mathbf{s}_0^T \mathbf{A}_i \mathbf{f}_{Ai} / \sigma_{\Delta i}^2 \quad (\text{E-9})$$

Therefore, substituting Equation (E-7) into (E-8) and comparing the result to Equation (E-9) shows that, if $n_i = 1$, then

$$\lambda_{RB}^2 = \lambda_i^2 \quad (\text{E-10})$$

This last result has also been demonstrated (in a different form, and using different methods) in [7, 8]. Interestingly, even though λ_i^2 in Equation (E-9) is a function of the state-dependent terms \mathbf{s}_0 and $\sigma_{\Delta i}^2$, it is actually independent of the state of interest when $n_i = 1$ (this becomes apparent because λ_i^2 is equal to λ_{RB}^2 , which is clearly not a function of the state of interest).

Finally, as expressed in Equations (15) and (28), q_{RB} and q_i both follow non-central chi-square distributions. These distributions have the same number of degrees of freedom if and only if $n - m = 1$, and they have the same non-centrality parameter if $n_i = 1$ (Equation (E-10)). Therefore, it is true that $q_{RB} = q_i$ if and only if $n_i = n - m = 1$.

APPENDIX F: COMPARISONS OF RB AND SS FAILURE MODE SLOPES

Comparison of RB versus SS Test Statistics

First, the worst-case slope squared for SS RAIM is expressed in Equation (31) as $\bar{g}_{Fi,SS}^2 = \sigma_{\Delta i}^2$. The subscript 'SS' was added for clarity of comparison with RB RAIM. In parallel, the worst-case slope squared under H_i is given in Equation (32), and for RB RAIM, it can be expressed as:

$$\bar{g}_{Fi,RB}^2 = \mathbf{s}_0^T \mathbf{A}_i (\mathbf{A}_i^T (\mathbf{I}_n - \mathbf{H}\mathbf{S}_0) \mathbf{A}_i)^{-1} \mathbf{A}_i^T \mathbf{s}_0 \quad (\text{F-1})$$

The term on the right hand side of Equation (F-1) has appeared earlier in Equation (E-5).

Therefore, for RB RAIM, the following equation is established:

$$\bar{g}_{Fi, RB}^2 = \sigma_{\Delta i}^2 \quad (\text{F-2})$$

Equations (31) and (F-2) prove that the worst-case slope squared is the same for both RAIM methods, and that it is equal to $\sigma_{\Delta i}^2$.

Generalization to Other Test Statistics for Single-SV Faults

Consider a detector that maps measurements into parity space, i.e., that provides direct observation of fault vector \mathbf{f} without being a function of \mathbf{x} . A straightforward choice is to express the detector's test statistic q as a linear combination of elements of the parity vector (i.e., a projection of the parity vector onto a given direction in parity space):

$$q = \mathbf{y}^T \mathbf{Q} \mathbf{z} = \mathbf{y}^T \mathbf{Q} (\mathbf{v} + \mathbf{f}) \quad (\text{F-3})$$

where \mathbf{Q} is defined in Equation (42) and \mathbf{y} is an $(n-m) \times 1$ unit vector, whose direction must be determined. Vector \mathbf{y} is defined with unit norm to avoid an extra normalization step when computing the test statistic q . For single-satellite faults, i.e., for $n_i=1$, following the same derivation that lead to Equation (D-10), the worst-case fault slope can be expressed as:

$$\bar{g}_{Fi}^2 = \mathbf{s}_0^T \mathbf{A}_i (\mathbf{A}_i^T \mathbf{Q}^T \mathbf{y} \mathbf{y}^T \mathbf{Q} \mathbf{A}_i)^{-1} \mathbf{A}_i^T \mathbf{s}_0 \quad (\text{F-4})$$

The best detector under H_i is found for the vector \mathbf{y} that minimizes \bar{g}_{Fi} , i.e., that maximizes the $n_i \times n_i$ matrix: $\mathbf{A}_i^T \mathbf{Q}^T \mathbf{y} \mathbf{y}^T \mathbf{Q} \mathbf{A}_i$. For $n_i=1$, $\mathbf{Q} \mathbf{A}_i$ is an $(n-m) \times 1$ vector, and the scalar $\mathbf{y}^T \mathbf{Q} \mathbf{A}_i$ is the inner product of \mathbf{y} with $\mathbf{Q} \mathbf{A}_i$, which is maximized when \mathbf{y} and $\mathbf{Q} \mathbf{A}_i$ are parallel. The unit direction vector for $\mathbf{Q} \mathbf{A}_i$ is defined as \mathbf{u}_i in Equation (46). It follows that \bar{g}_{Fi} is minimized when \mathbf{y} coincides with \mathbf{u}_i . According to Appendix G, the detector matrix $\mathbf{y}^T \mathbf{Q} = \mathbf{u}_i^T \mathbf{Q}$, which is here designed to minimize the worst-case fault slope \bar{g}_{Fi} , is actually equivalent to the SS detector $\mathbf{s}_{\Delta i}^T / \sigma_{\Delta i} = \mathbf{u}_i^T \mathbf{Q}$. This shows that, for single-SV faults, the SS test statistic minimizes \bar{g}_{Fi} .

In addition, the first part of this appendix proved that \bar{g}_{Fi} was the same for RB and SS RAIM. Therefore, for single-SV faults, this appendix has demonstrated that both RB and SS minimize \bar{g}_{Fi} .

APPENDIX G: PROOF THAT NORMALIZED SOLUTION SEPARATIONS ARE PROJECTIONS OF THE PARITY VECTOR ON FAULT MODE LINES

This appendix provides a proof that, for single-measurement faults, i.e., for $n_i=1$, the n solution

separations q_i , for $i=1, \dots, n$, are projections of the parity vector on their corresponding single-measurement fault mode lines. In mathematical form, we present a derivation for Equation (49), which is rewritten as:

$$\frac{\mathbf{s}_{\Delta i}^T}{\sigma_{\Delta i}} \mathbf{z} = \frac{\mathbf{A}_i^T \mathbf{Q}^T}{\sqrt{\mathbf{A}_i^T \mathbf{Q}^T \mathbf{Q} \mathbf{A}_i}} \mathbf{Q} \mathbf{z} \quad (\text{G-1})$$

This derivation assumes single-measurement faults: $n_i=1$. For example, for a fault on the first measurement, Equation (18) becomes:

$$\mathbf{A}_i = \begin{bmatrix} 1 \\ \mathbf{0}_{(n-1) \times 1} \end{bmatrix} \text{ and } \mathbf{B}_i = \begin{bmatrix} \mathbf{0}_{1 \times (n-1)} \\ \mathbf{I}_{n-1} \end{bmatrix} \quad (\text{G-2})$$

The measurement vector \mathbf{z} can be broken down into two components corresponding to the faulted measurement, and to the fault-free measurement subset. \mathbf{z} is expressed as:

$$\mathbf{z} = (\mathbf{A}_i \mathbf{A}_i^T + \mathbf{B}_i \mathbf{B}_i^T) \mathbf{z} \quad (\text{G-3})$$

Substituting Equation (G-3) into (G-1), and identifying in the resulting expression the row vectors, pre-multiplying $\mathbf{A}_i^T \mathbf{z}$ and $\mathbf{B}_i^T \mathbf{z}$ provides two equations, which can be written as:

$$\frac{\mathbf{s}_{\Delta i}^T}{\sigma_{\Delta i}} \mathbf{A}_i = \frac{\mathbf{A}_i^T \mathbf{Q}^T \mathbf{Q} \mathbf{A}_i}{\sqrt{\mathbf{A}_i^T \mathbf{Q}^T \mathbf{Q} \mathbf{A}_i}} = (\mathbf{A}_i^T \mathbf{Q}^T \mathbf{Q} \mathbf{A}_i)^{\frac{1}{2}} \quad (\text{G-4})$$

$$\frac{\mathbf{s}_{\Delta i}^T}{\sigma_{\Delta i}} \mathbf{B}_i = \frac{\mathbf{A}_i^T \mathbf{Q}^T \mathbf{Q} \mathbf{B}_i}{\sqrt{\mathbf{A}_i^T \mathbf{Q}^T \mathbf{Q} \mathbf{A}_i}} \quad (\text{G-5})$$

The remainder of this appendix aims at showing that these two equations are satisfied, which is proof of Equation (G-1).

Step 1 Proof of Equation (G-4)

It was shown in Equation (E-5) that:

$$\sigma_{\Delta i}^2 = \mathbf{s}_0^T \mathbf{A}_i (\mathbf{A}_i^T (\mathbf{I}_n - \mathbf{H} \mathbf{S}_0) \mathbf{A}_i)^{-1} \mathbf{A}_i^T \mathbf{s}_0 \quad (\text{G-6})$$

Since \mathbf{A}_i is an $n \times 1$ vector in this appendix, and since $(\mathbf{I}_n - \mathbf{H} \mathbf{S}_0)$ is idempotent, the term under the inversion is an inner product of a vector with itself, and hence it is a positive scalar. Thus, the standard deviation of the solution separation can be written as:

$$\sigma_{\Delta i} = \mathbf{s}_0^T \mathbf{A}_i (\mathbf{A}_i^T (\mathbf{I}_n - \mathbf{H} \mathbf{S}_0) \mathbf{A}_i)^{-\frac{1}{2}} \quad (\text{G-7})$$

Substituting Equation (45) into (G-7) results in:

$$\sigma_{\Delta i} = \mathbf{s}_0^T \mathbf{A}_i (\mathbf{A}_i^T \mathbf{Q}^T \mathbf{Q} \mathbf{A}_i)^{-\frac{1}{2}} \quad (\text{G-8})$$

In addition, substituting Equation (D-2) (i.e., $\mathbf{s}_{\Delta i}^T \mathbf{A}_i = \mathbf{s}_0^T \mathbf{A}_i$) into (G-8), and recalling that $\mathbf{A}_i^T \mathbf{Q}^T \mathbf{Q} \mathbf{A}_i$ is a scalar, we obtain an expression that is equivalent

to (G-4) and therefore concludes the first step of this derivation.

Step 2 Proof of Equation (G-5)

Multiplying both sides of Equation (G-5) by $(\mathbf{A}_i^T \mathbf{Q}^T \mathbf{Q} \mathbf{A}_i)^{1/2}$ and substituting Equation (G-4) for

$(\mathbf{A}_i^T \mathbf{Q}^T \mathbf{Q} \mathbf{A}_i)^{1/2}$ into the resulting expression yields the following equation:

$$\mathbf{A}_i^T \frac{\mathbf{s}_{\Delta i} \mathbf{s}_{\Delta i}^T}{\sigma_{\Delta i}^2} \mathbf{B}_i = \mathbf{A}_i^T \mathbf{Q}^T \mathbf{Q} \mathbf{B}_i \quad (\text{G-9})$$

Multiplying both sides of Equation (G-9) by $\sigma_{\Delta i}^2$, using the definition of $\sigma_{\Delta i}^2$ in Equation (26), and substituting Equation (45) into (G-9), we obtain:

$$\mathbf{A}_i^T \mathbf{s}_{\Delta i} \mathbf{s}_{\Delta i}^T \mathbf{B}_i = (\alpha^T \mathbf{P}_{\Delta i} \alpha) \mathbf{A}_i^T (\mathbf{I}_n - \mathbf{H} \mathbf{S}_0) \mathbf{B}_i \quad (\text{G-10})$$

The left-hand side of Equation (G-10) is modified in two steps. First, substituting Equation (10) into (D-2) provides the following result:

$$\mathbf{A}_i^T \mathbf{s}_{\Delta i} = \mathbf{A}_i^T \mathbf{s}_0 = \mathbf{A}_i^T \mathbf{S}_0^T \alpha = \mathbf{A}_i^T \mathbf{H} \mathbf{P}_0 \alpha \quad (\text{G-11})$$

Then, using the definitions of $\mathbf{s}_{\Delta i}$ in Equation (25), and of \mathbf{s}_0 and \mathbf{s}_i in Equations (10) and (20), respectively, it is shown that:

$$\begin{aligned} \mathbf{s}_{\Delta i}^T \mathbf{B}_i &= (\mathbf{s}_0^T - \mathbf{s}_i^T) \mathbf{B}_i \\ &= \alpha^T (\mathbf{S}_0 - \mathbf{S}_i) \mathbf{B}_i \\ &= \alpha^T (\mathbf{P}_0 \mathbf{H}^T - \mathbf{P}_i \mathbf{H}^T \mathbf{B}_i \mathbf{B}_i^T) \mathbf{B}_i \\ &= \alpha^T (\mathbf{P}_0 - \mathbf{P}_i) \mathbf{H}^T \mathbf{B}_i \\ &= -\alpha^T \mathbf{P}_{\Delta i} \mathbf{H}^T \mathbf{B}_i \end{aligned} \quad (\text{G-12})$$

where we used:

$$\mathbf{B}_i^T \mathbf{B}_i = \mathbf{I}_{n-1} \quad (\text{G-13})$$

and we used the definition of $\mathbf{P}_{\Delta i}$ in Equation (26).

In addition, it is worth remembering Equation (D-2):

$$\mathbf{A}_i^T \mathbf{B}_i = \mathbf{0}_{1 \times (n-1)}. \quad (\text{G-14})$$

Substituting Equations (G-11), (G-12) and (G-14) into (G-10), Equation (G-10) becomes:

$$\mathbf{A}_i^T \mathbf{H} \mathbf{P}_0 \alpha \alpha^T \mathbf{P}_{\Delta i} \mathbf{H}^T \mathbf{B}_i = (\alpha^T \mathbf{P}_{\Delta i} \alpha) \mathbf{A}_i^T \mathbf{H} \mathbf{P}_0 \mathbf{H}^T \mathbf{B}_i \quad (\text{G-15})$$

Taking the dot product of the $1 \times (n-1)$ row vector in (G-15) with the $(n-1) \times 1$ vector $\mathbf{B}_i^T \mathbf{H} \mathbf{P}_0 \alpha$, and using the definition of \mathbf{P}_i in Equation (20), we obtain:

$$\mathbf{A}_i^T \mathbf{H} \mathbf{P}_0 \alpha \alpha^T \mathbf{P}_{\Delta i} \alpha = (\alpha^T \mathbf{P}_{\Delta i} \alpha) \mathbf{A}_i^T \mathbf{H} \mathbf{P}_0 \alpha \quad (\text{G-16})$$

Noticing that $(\alpha^T \mathbf{P}_{\Delta i} \alpha)$ is a scalar, Equation (G-16) is always true, and since it is equivalent to (G-5), the proof of this appendix is established.

REFERENCES

1. Lee, Y. C., "Analysis of Range and Position Comparison Methods as a Means to Provide GPS Integrity in the User Receiver," *Proceedings of the 42nd Annual Meeting of The Institute of Navigation*, Seattle, WA, 1986, pp. 1–4.
2. Parkinson, B. W. and Axelrad, P., "Autonomous GPS Integrity Monitoring Using the Pseudorange Residual," *NAVIGATION*, Vol. 35, No. 2, Summer 1988, pp. 225–274.
3. Potter, I. E. and Suman, M. C., "Threshold-less Redundancy Management With Arrays of Skewed Instruments," *AGARDOGRAPH - No 224*, 1977, pp. 15–11 to 15–25.
4. Sturza, M., "Navigation System Integrity Monitoring Using Redundant Measurements," *NAVIGATION*, Vol. 35, No. 4, Winter 1988–1989, pp. 483–502.
5. Brenner, M., "Integrated GPS/Inertial Fault Detection Availability," *Proceedings of the 8th International Technical Meeting of the Satellite Division of The Institute of Navigation (ION GPS 1995)*, Palm Springs, CA, September 1995, pp. 1949–1958.
6. Brown, R. Grover, "A Baseline GPS RAIM Scheme and a Note on the Equivalence of Three RAIM Methods," *NAVIGATION*, Vol. 39, No. 3, Fall 1992, pp. 301–316.
7. Blanch, J., Ene, A., Walter, T., and Enge, P., "An Optimized Multiple Hypothesis RAIM Algorithm for Vertical Guidance," *Proceedings of the 20th International Technical Meeting of the Satellite Division of The Institute of Navigation (ION GNSS 2007)*, Fort Worth, TX, September 2007, pp. 2924–2933.
8. Chan, F-C. and Pervan, B., "A Practical Approach to RAIM-based Fault-Tolerant Position Estimation," *Proceedings of the 23rd International Technical Meeting of the Satellite Division of The Institute of Navigation (ION GNSS 2010)*, Portland, OR, September 2010, pp. 3181–3190.
9. EU-US Cooperation on Satellite Navigation, WG C-ARAIM Technical Subgroup, "ARAIM Technical Subgroup Milestone 1 Report," 2012. Available online: http://ec.europa.eu/enterprise/newsroom/cf/_getdocument.cfm?doc_id=7793, [accessed December 04, 2014].
10. RTCA Special Committee 159, "Minimum Aviation System Performance Standards for the Local Area Augmentation System (LAAS)," *RTCA/DO-245*, 2004, Appendix D.
11. Angus, J. E., "RAIM with Multiple Faults," *NAVIGATION*, Vol. 53, No. 4, Winter 2006–2007, pp. 249–257.
12. Joerger, M. and Pervan, B., "Kalman Filter-Based Integrity Monitoring Against Sensor Faults," *AIAA Journal of Guidance, Control and Dynamics*, Vol. 36, No. 2, March–April 2013, pp. 349–361.
13. Blanch, J., Walter, T., and Enge, P., "Results on the Optimal Detection Statistic for Integrity Monitoring," *Proceedings of the 2013 International Technical Meeting of The Institute of Navigation*, San Diego, California, January 2013, pp. 262–273.
14. Joerger, M., Stevanovic, S., Chan, F-C., Langel, S., and Pervan, B., "Integrity Risk and Continuity Risk for Fault Detection and Exclusion Using Solution

- Separation ARAIM,” *Proceedings of the 26th International Technical Meeting of the Satellite Division of The Institute of Navigation (ION GNSS+ 2013)*, Nashville, TN, September 2013, pp. 2702–2722.
15. van Graas, F. and Farrell, J., “Baseline Fault Detection and Exclusion Algorithm,” *Proceedings of the 49th Annual Meeting of The Institute of Navigation*, Cambridge, MA, June 1993, pp. 413–420.
 16. DeCleene, B., “Defining Pseudorange Integrity – Overbounding,” *Proceedings of the 13th International Technical Meeting of the Satellite Division of The Institute of Navigation (ION GPS 2000)*, Salt Lake City, UT, 2000, pp. 1916–1924.
 17. Pervan, B., Navigation Integrity for Aircraft Precision Landing using the Global Positioning System, Ph.D. Dissertation, Stanford University, March 1996.
 18. Lee, Y. C., personal conversation in March 2014.
 19. Drezner, Z. and Wesolowsky, G. O., “On the Computation of the Bivariate Normal Integral,” *Journal of Statistical Computation and Simulation*, Vol. 35, 1989, pp. 101–107.
 20. Joerger, M., Chan, F.-C., Langel, S., and Pervan, B., “RAIM Detector and Estimator Design to Minimize the Integrity Risk,” *Proceedings of the 25th International Technical Meeting of the Satellite Division of The Institute of Navigation (ION GNSS 2012)*, Nashville, TN, September 2012, pp. 2785–2807.
 21. Blanch, J., Walter, T., and Enge, P., “Optimal Positioning for Advanced RAIM,” *Proceedings of the 2012 International Technical Meeting of The Institute of Navigation*, Newport Beach, CA, January 2012, pp. 1624–1647.